SEARCH FOR THE DECAY
$Ds \rightarrow \omega\, l\nu$

by

JIN ZHU

DISSERTATION

Submitted to the Graduate School

of Wayne State University,

Detroit, Michigan

in partial fulfillment of the requirements

for the degree of

DOCTOR OF PHILOSOPHY

2010

MAJOR: PHYSICS

Approved by:

_____

Advisor Date

_____

_____

_____

_____

ACKNOWLEDGMENTS

Doing PhD is a life time experience and could be challenging to accomplish. I've been extremely lucky to come to this point: lucky to travel over ten thousand miles to Detroit; lucky to receive insightful guidance from professors at Wayne State University; lucky to be part of a collaborative workgroup and most importantly, so lucky to have a family who support my work without any hesitation. It is impossible to express all my gratitude and appreciation on this page. I'll try to elaborate a few with my poor english.

I would like to first express my greatest gratitude to my advisor Giovanni Bonvinici. He is simply the best teacher I've ever met. He is such a good teacher that he never seemed to be tired of repeating questions. He never called any question a stupid one and has always given me positive feedbacks. He is such enthusiastic about his research and always works late for me and his research. During my graduate study at Wayne State, I was deeply impressed and influenced by his diligence, his positive attitude and his ability to grasp physics details. Other than that, he is such a nice person who teach me to behave like a gentleman and how to deal with different things. If there's a list of people who have helped me so much that I could never repay them properly. Giovanni is the one on my top list. I wish he finds much success at Belle group.

I would also like to thank our group members at Wayne State University. Thank you to professor David Cinabro. His willingness and ability too add insight to complicate questions have helped me a lot on this thesis. Thanks to our group member Adam Lincoln for answering a lot of CLEO questions. Thanks for the discussions with group member Peng Zhou and Smith Mackenzie. I would also like to thank teachers and professors at Wayne State. I've learned a lot from classes and colloquiums at Wayne State. Thanks to professor Jogindra Wadehra and David Cinabro for writing

reference letters for me. Thanks to my committee members for their support and suggestions.

Many thanks to the CLEO members-those who I known and who I couldn't name of. I would like to thank the CLEO101 teachers who taught me the first step of data analysis. I would also like to thank Jonathan Insler for sharing part of his code and result with me as a crosscheck. I appreciate Chul Su Park and Fan Yang for help on my analysis. I also thank previous CLEO students. I borrowed some ideas from their thesis when I was writing first two chapters of my thesis.

I would like to thank many friends at Wayne State University. I've had a lot of fun with them and I really cherish the time with them. Thanks to pastor David Chang and people at the Central Alliance Church. Their warm help eased my loneness and when I came to Detroit four years ago.

Last, I would also like to take a moment to thank my family members who had supported me throughout these many years, and who are now celebrating with me in spirit. Their patience, love and encouragement has made this work not so hard to finish. Thank you to my wife Han Chen, my father and my mother. Without having them to share this moment with me, it would have no meaning or satisfaction at all. I love you all!

TABLE OF CONTENTS

LIST OF TABLES

LIST OF FIGURES

Chapter 1: Introduction

1.1 Standard Model

The Standard Model describes properties of fundamental particles and their interactions. Standard Model is a quantum field theory developed in the 1960's and 70's to encompass electroweak and strong interactions based on local gauge invariance and $SU(3) \times SU(2) \times SU(1)$ symmetry[1][2][3]. The Standard Model incorporates the quarks and the leptons (the electron and its relatives) into a successful framework that has proven to be very rugged and reliable by many experiments. In the Standard Model, quarks and leptons are said to be fundamental and structureless. They are point-like and indivisible while possessing some intrinsic property such as spin, charge, color, etc. All fundamental particles can be arranged into three groups: quarks, leptons, and gauge bosons (force carriers or mediators). The remaining particle, the Higgs boson, is the last remaining particle of the Standard Model yet to be discovered. It plays a key role in explaining the mass of the other particles, specifically the large mass difference between the photon, the vector bosons and the quarks. The gravitational force is not part of the Standard Model and will not be discussed here.

1.1.1 Quarks and Leptons

Quarks and anti-quarks are the fundamental components of hadrons, either in the form of quark-antiquark pairs ($q\bar{q}$) called mesons, like $\pi^{\pm}$, $K^{\pm}$ and the D_s^+, or 3-quark combinations ($q_i q_j q_k$) called baryons, like the proton and neutron. The concept that all hadrons can be built out of two basic combinations of quarks and antiquarks is also called the Standard Model (of hadrons), although, as we will see later, it has

Family	Name	Charge	Mass
I	u	$+\frac{2}{3}$	1-4 MeV
	d	$-\frac{1}{3}$	4-8 MeV
II	c	$+\frac{2}{3}$	1.15-1.35GeV
	s	$-\frac{1}{3}$	$80 - 130MeV$
III	t	$+\frac{2}{3}$	174GeV
	b	$-\frac{1}{3}$	$4.1 - 4.4GeV$

Table 1.1: Quarks in the Standard Model

come under increasing attack due to relatively recent discoveries.

Quarks come in six types, which can be split into three generations. The first generation of quarks consists of the up (u) and down (d). Together with the electron the first generation of quarks make up all the ordinary matter around us. The second generation (strange (s) and charm (c) quarks) and the third generation (bottom (b) and top (t) quarks) are the rest of the known quarks. Since they have intrinsic angular momentum of $\frac{1}{2}\hbar$, all quarks are fermions. Some properties of the quarks are shown in Table 1.1. Quarks are never individually observed but rather are seen only in hadrons. Quarks also come in three colors (referring to the strong force charge), with each color quark considered distinct: for example, there is a red up quark, a blue up quark and a green up quark. A gluon exchange can transform the quark into a different color quark of the same type. The strong force conserves the quantum numbers D, U, S, C, B, and T, which are associated with the six quark flavors. In contrast, the weak force does not conserve those quantum numbers.

The leptons also come in six types which are listed in Table 1.2 along with their corresponding masses and charges. Every lepton also has an anti-particle with the same mass but opposite charge and quantum numbers. All leptons have intrinsic angular momentum, or spin, of $\frac{1}{2}\hbar$ and are therefore fermions. They interact via the electro-weak force but not via the strong force. The lightest charged lepton is the familiar electron. The muon (μ) and tau (τ) have the same general properties as the electron, but with larger masses. These heavier versions are unstable and

Family	Name	Charge	Mass
I	e	-1	0.511MeV
	ν_e	0	< 2eV
II	μ	-1	106MeV
	ν_μ	0	< 0.19MeV
III	τ	-1	1.78GeV
	ν_τ	0	< 18.2MeV

Table 1.2: Leptons in the Standard Model

Force	Name	Charge	Mass
EM	photon(γ)	0	0
Weak	$W^\pm$	± 1	80.40GeV
	Z^0	0	91.188
Strong	gluon(g)	0	0

Table 1.3: Gauge bosons in the Standard Model

therefore not found in ordinary matter. The neutrinos are neutral particles that interact only through the weak force (ν_e, ν_μ and ν_τ) . Together each lepton and its accompanying neutrino form a generation. Each generation of leptons (say, electron and its associated neutrino ν_e) has its own quantum number which is conserved. An electron cannot be destroyed without creating an electron or electron neutrino. Recent experiments show that one neutrino generation can mix with another neutrino generation. This violates the lepton number conservation law.

1.1.2 Forces and Mediators

Interactions, or forces, among fundamental particles are divided into 4 types: strong, weak, electromagnetic, and gravitational. Of these, gravity is by far the weakest and is not part of the Standard Model. In the Standard Model the three remaining forces are represented as the exchange of gauge bosons between interacting particles. All gauge bosons have integer spin, and some of their properties are shown in Table 1.3.

The classical formulation of electromagnetism is Maxwell's equations, while its quantum version is Quantum Electrodynamics (QED). QED deals with the interac-

tions between photons and electrically charged particles, and has been extensively tested. It is to date the most accurate and precise theory in all physics. The photon is a massless mediator of the electromagnetic field, which consequently gives the electromagnetic force infinite range. Electromagnetic fields are best known for binding nuclei and electrons inside the atom, and as the oscillating electric and magnetic fields that make light waves.

Weak interactions were first formulated in nuclear decays and were represented by a "black box" interaction. All fundamental fermions, including the neutrinos, participate in the weak interaction. The weak nuclear force is now described as being mediated by the $W^{\pm}$ and Z^0 bosons and interacts with leptons, quarks and weak bosons themselves. The $W^{\pm}$ and Z^0 bosons are very massive and have a relatively short range. Interacting with the $W^{\pm}$ boson change one type of quark or lepton into another. These changes can lead to spontaneous decays of the type $\mu^- \rightarrow e^- \bar{\nu}_e \nu_\mu$.The Z^0 has interactions much like the photon and cannot change types of quarks or leptons. The fact that the Z^0 and the photon have similar interactions at high energies is a major confirmation of the unification of the weak force and QED in the Standard Model. The weak force and QED are different expressions of the electroweak force in the low-energy limit.

The quantum theory which describes the strong force is known as quantum chromodynamics (QCD). QCD is mediated by gluons and interacts with color charge; in this case, "color" does not refer to the electromagnetic spectrum but is merely a name for the type of charge carried by quarks and gluons. Unlike electric charge, of which there is only one kind with values of ± 1, color charge comes in three favors, denoted "R", "G", and "B" and each can have values of ± 1. Quarks have a color charge, antiquarks have anticolor charge. Leptons have no color, and gluons have a color/anti-color charge (such as $R\bar{G}$ or more generally, $c_i \bar{c_j}$). An object is colorless, or white, if the colors comprising it are included in any of the following ways: red,

blue, and green in equal amounts; or equal amounts of a color and its anticolor. The strong force has the unique property that no observable state is allowed to have a color other than white. This is called color confinement and as a result, no single quark is observable. Instead, combinations of quarks (hadrons) are the observable states. The strong force, unlike gravity and the electroweak force, becomes stronger as the separation between color-charged objects increases. Of the fundamental fermions, only the quarks can interact through the action of strong force.

Another interesting aspect of QCD is asymptotic freedom[4][5]. As the momentum transferred in an interaction increases, the strength, or coupling, in the interaction decreases. Therefore, in these types of interactions, perturbative methods can be applied to the calculations, as they are in QED. However, because the strength of the interaction increases at lower momenta, QCD calculations are very difficult in most cases.

1.2 Symmetries

Physics is deeply concerned with symmetries. Emmy Noether developed a theorem [6] that any conserved quantity must be related to a symmetry in nature. For instance, if the laws of Nature are invariant under spatial translation, this necessarily implies conservation of linear momentum. If the laws of Nature are invariant over time, conservation of energy is implied.

Parity invariance for a process means that process is the same in a mirror image (where one spatial axis is reversed), or if all three spatial axes are reversed. Parity can only assume ± 1 values, sometimes called even and odd parity. A process that conserves parity can only transform a system with even parity to another system with even parity, and odd to odd. Particles carry intrinsic parity, which reflects the construction of the particle's wave function. The lowest mass hadrons, such as pions and kaons,have zero angular momentum and have odd parity. The parity of a group of

particles depends on the intrinsic parity of the particles and the angular momentum they share; for example, the eigenvalue of the parity operator on a group of n pions with total angular momentum L is $(-1)^{n+L}$.

Until the 1950's, scientists believed that all processes conserved parity. Lee and Yang [7] were the first to examine the evidence for parity conservation, and found that parity was conserved in all cases for strong and electromagnetic interactions but that there was no evidence of parity conservation in weak interactions. In fact, there was a possible counterexample in the θ^+ and τ^+(now considered the same particle, K^+). These two particles had the same mass and charge but decayed to different final states: $\theta^+ \rightarrow 2\pi$, an even parity state, and $\tau^+ \rightarrow 3\pi$, an odd parity state. Accepting the possibility that weak decays do not require parity conservation allows the common-sense deduction that the θ^+ and τ^+, having the same mass and charge, are the same particle with different decays. Lee and Yang formulated an experiment that was conducted by Wu[8] to verify parity conservation. The experiment, simple in concept though challenging technically, is to take a sample of radioactive ^{60}Co and align their spins along a chosen direction. When an atom undergoes beta decay, the direction of the electron is measured. The surprising result was that there is a preferred direction for the emission of the electron, which is the direction of the nuclear spin.

In the experiment, one then flips the spin in the opposite direction. If parity were conserved, the electron would still be emitted in the original direction, which is now opposite to the spin. If the weak force respected parity, Wu would have observed equal proportions of electrons aligned and anti-aligned with the spin, but that was not the case.

1.3 Quark mixing

At the time that quark theory was first introduced by Gell-Mann and Zweig, it contained no concept of quark generations. The quark types in the theory at the time, the up, down, and strange quarks, were combined to make hadrons that could be classified based on electric charge and strangeness. There was no experimental reason for any additional quarks, but Bjorken and Glashow[9], as a way of making nature more symmetrical at a time when there were three known quarks and four known leptons, predicted the existence of the yet-to-be discovered charm (c) quark.

Cabibbo[10] hypothesized in 1963 that weak interaction cross-sections involving quarks could be described in the same way as weak interaction cross-sections involving electrons and neutrinos, with only an additional factor in the amplitude. This factor was $\cos\theta_C$ for particles with a down- up interaction and $\sin\theta_C$ for particles undergoing a strange-up interaction. θ_C came to be known as the Cabibbo angle with an experimental value of 13.1°, or 0.229.

Quark-quark interactions that proceed through the larger amplitude proportional to $\cos\theta_C$ are called Cabibbo favored. Quark-quark interactions that proceed through the smaller amplitude proportional to $\sin\theta_C$ are called Cabibbo suppressed.

This theory failed when applied to the decay rate amplitude of $K^0 \rightarrow \mu^+\mu^-$. It was predicted to be the same as a leptonic decay with four weak lepton interactions, with an additional factor of $sin\theta_C cos\theta_C$. Instead, the actual rate is tiny, with a branching fraction of less than 10^{-7}. To solve this problem, Glashow, Iliopoulos, and Maiani [11] looked back to the earlier idea by Glashow and Bjorken that there should be a fourth quark (named "charm") to balance with the four known leptons. This fourth quark could then be used to cancel the amplitude of $K^0 \rightarrow \mu^+\mu^-$ if its couplings were $cos\theta_C$ for particles in a strange-charm weak interaction and $-sin\theta_C$for particles in a down-charm weak interaction.

Adding a fourth quark with similar rotations in flavor space suggests that the

weak force interactions with quarks could be more simply portrayed as operating on a rotation of the s and d quarks. It can be expressed as:

$$\begin{pmatrix} d' \\ s' \end{pmatrix} = \begin{pmatrix} cos\theta_C & sin\theta_C \\ -sin\theta_C & cos\theta_C \end{pmatrix} \begin{pmatrix} d \\ s \end{pmatrix} \tag{1.1}$$

Here, d' and s' are the states that the weak force interacts with, a mixture of flavor states d and s. Kobayashi and Maskawa [12] expanded this mixing matrix to encompass a third generation, the bottom and top quarks, in order to introduce imaginary terms generating CP violation. This mixing matrix (CKM matrix) is composed of the amplitudes for down-type quarks interacting with up-type quarks:

$$\begin{pmatrix} d' \\ s' \\ b' \end{pmatrix} = \begin{pmatrix} V_{ud} & V_{us} & V_{ub} \\ V_{cd} & V_{cs} & V_{cb} \\ V_{td} & V_{ts} & V_{tb} \end{pmatrix} \begin{pmatrix} d \\ s \\ b \end{pmatrix} \tag{1.2}$$

V is minimally described by three angles and one phase:

$$V = \begin{pmatrix} c_1 & s_1c_3 & s_1s_3 \\ -s_1c_2 & c_1c_2c_3 - s_2s_3e^{i\delta} & c_1c_2s_3 + s_2c_3e^{i\delta} \\ -s_1s_2 & c_1s_2c_3 + c_2s_3e^{i\delta} & c_1s_2s_3 - c_2c_3e^{i\delta} \end{pmatrix} \tag{1.3}$$

where s and c here denote sine and cosine respectively, while the subscript identifies the angle. The CP-violating phase is δ. Some prefer to work in the Wolfenstein parameterization[13], an expansion of the mixing matrix in $V_{us} = 0.226$, denoted by λ. The Wolfenstein parameterization is shown here to $O(\lambda^3)$.

$$V \simeq \begin{pmatrix} 1 - \frac{1}{2}\lambda^2 & \lambda & A\lambda^3(\rho - i\eta) \\ -\lambda & 1 - \frac{1}{2}\lambda^2 & A\lambda^2 \\ A\lambda^3(1 - \rho - i\eta) & -A\lambda^2 & 1 \end{pmatrix} \tag{1.4}$$

The current experimental values [14] for the mixing matrix are

$$V \simeq \begin{pmatrix} 0.9738 \pm 0.0003 & 0.226 \pm 0.002 & (4.3 \pm 0.3) \times 10^{-3} \\ 0.230 \pm 0.011 & 0.957 \pm 0.095 & (41.6 \pm 0.6) \times 10^{-3} \\ (7.4 \pm 0.8) \times 10^{-3} & 4.81^{+0.18}_{-0.14} \times V_{td} & > 0.78 \end{pmatrix}. \quad (1.5)$$

1.4 Charm quark and D (Ds) meson

In November 1974 two different groups, at Brookhaven [15] and at SLAC [16], published papers announcing their simultaneous discovery of a new particle with mass around $3.1 GeV$ and a lifetime of at least a 1000 times longer than that of similarly massive particles. This new particle was named J/ψ and was identified as the $^3S_1$ state of $(c\bar{c})$. States containing only charm quarks and antiquarks are collectively called charmonium.

This opened the field of charm spectroscopy, with new hadrons equivalent to those one can construct with the lower mass quarks. Amongst them the D^0 and D^+ mesons, which contain a c quark and a $\bar{u}$ and $\bar{d}$ antiquark respectively. The D_s meson is the lowest mass hadron containing a c quark and $\bar{s}$ antiquark. They all have the same angular momentum and parity as the pion or the kaon, having the same, lowest energy spin and orbit configuration, and are collectively called the D_s mesons. Fig 1.1 shows the typical Feynman diagrams of D_s decay with (a) being Cabblibo-favored decay, (b) and (c): Cabbibo-suppressed decay, (d): double Cabbibo-suppressed decay and (e) and (f): annihilation decay.

The D mesons live for times of the order 1psec before decaying weakly, which means they fly a distance from the Interaction Point before decaying. The detection of a detached "vertex", or candidate point for a seconday source of particles, play an important role in D analysis at higher energy accelerators. There, the D mesons can fly for hundreds of microns to centimeters before decaying, and powerful but

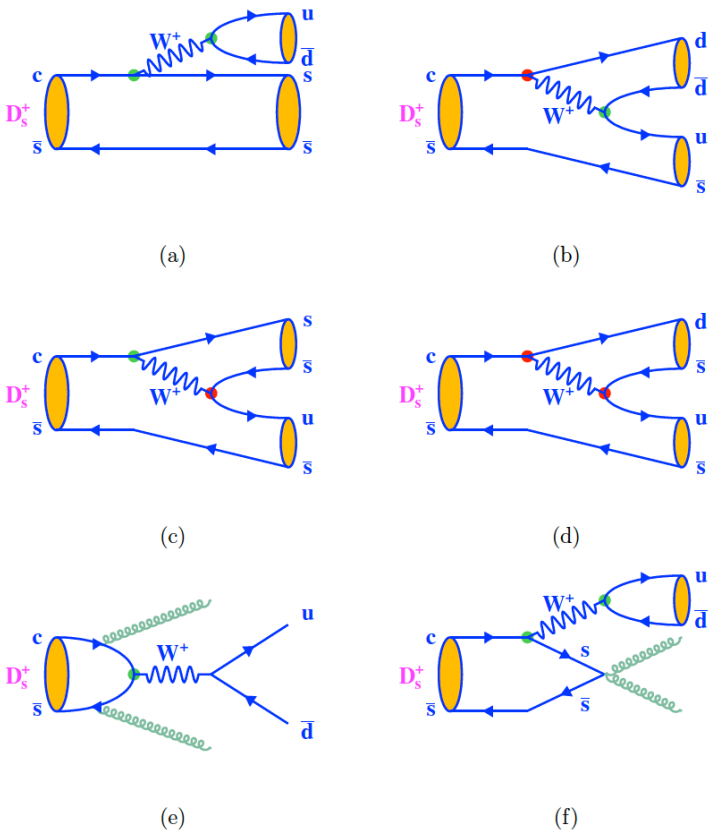

Figure 1.1: Feynman diagrams of typical D_s meson decay.

heavy Vertex Detectors routinely detect such secondary vertices. However, at the low energy of CLEO-c the D only travel for 10-100μm, making vertex detection impossible. The heavy Vertex Detector of CLEO II.V was replaced with a lighter particle detector when the detector was upgraded to CLEO-c in 1999. By giving up on vertex detection, CLEO-c was made lighter and therefore better at transmitting particles to the outher layers of CLEO with minimal degradation due to particle interactions with the detector material.

Numerous excited states (states with higher orbital number and higher mass) exist for all these mesons. The next highest in mass are generically called D^*, or D^{*0}, D^{*+}, D_s^* respectively. All these have spin one and can decay to the ground state by emitting a pion or photon.

1.5 The topic of this thesis.

An important line of theoretical QCD research in the last 30 years, first introduced by Brodsky and collaborators, has been an alternative expression of the hadron wavefunction[17][18]. Ignoring states containing a gluon, such as $|u\bar{s}g>$ and $|u\bar{s}q\bar{q}g>$, the Fock states of, for example, the K^+ meson reads

$$|K^+>= a_0|u\bar{s}> +a_1|u\bar{s}q\bar{q}> +a_2|u\bar{s}q\bar{q}q\bar{q}> +... \tag{1.6}$$

The a_i coefficients are such that $\Sigma a_i^2 = 1$, so that the Standard Model of hadrons is recovered when $a_0 = 1$. The physical interpretation of the Fock development is that the hadron is a coherent superposition of states of different multiplicity.

Long considered a fringe idea by mainstream physicists, this representation of hadrons nevertheless gained a growing support in the theoretical community over the years. The higher number of degrees of freedom in the wavefunction representation helped accommodate a growing body of observed, exotic QCD phenomena.

Fock states have gained widespread acceptance with the discovery of new charmonium states [19, 20, 21, 22], although competing models (such as the "hadron molecule", or pure 4-quark states) are also pursued [23, 24, 25, 26, 27, 28, 29, 30, 31].

If one accepts the Fock development as a true picture of the hadrons, the same questions outlined in the previous Section remain: how do the a_i coefficients depend on the mass of the valence quarks, the mass of the extra quark pair, their momentum, and the coupling constant?

This thesis probes the 4-quark component of the D_s (its a_1 component in Eq. 1.6) by looking for the decay $D_s \to \omega e\nu$. Assuming that the ω is a pure 2-quark state, its valence quarks are distinct from those of the D_s, and the decay can proceed through the diagram of Fig 1.2.

Here, both initial valence quarks annihilate while a lepton pair is produced. Nei-

ther Cabibbo favored, nor Cabibbo suppressed, decays can contribute to this final state. This process, first discussed in Ref.[32], has not been estimated directly, but Ref. [33] estimates the theoretical branching ratio for the equivalent decay $B^+ \rightarrow \psi l \nu$.

The advantage of the method is obvious. Known weak decays do not contribute to this final state. The lepton pair effectively eliminates the valence quarks, leaving the other quarks for observation.

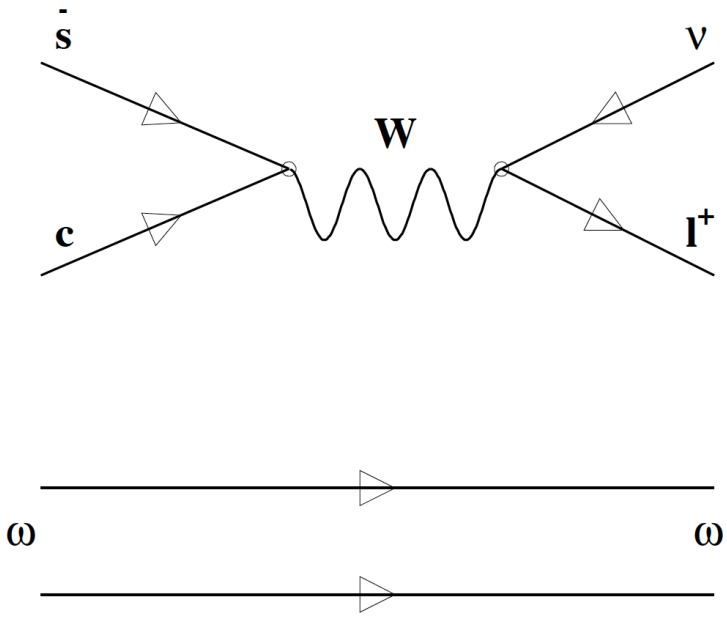

Figure 1.2: 4-quark semileptonic decay of the D_s meson.

Recent work by Gronau and Rosner [34] also suggests that the decay can proceed through $\omega - \phi$ mixing(see Fig 1.3). They quote an expected branching ratio of $(0.13 \pm 0.05)\%$, assuming that such mixing exists. Clearly, more than one independent measurement of this type will have to be performed if the two models are to be sorted out.

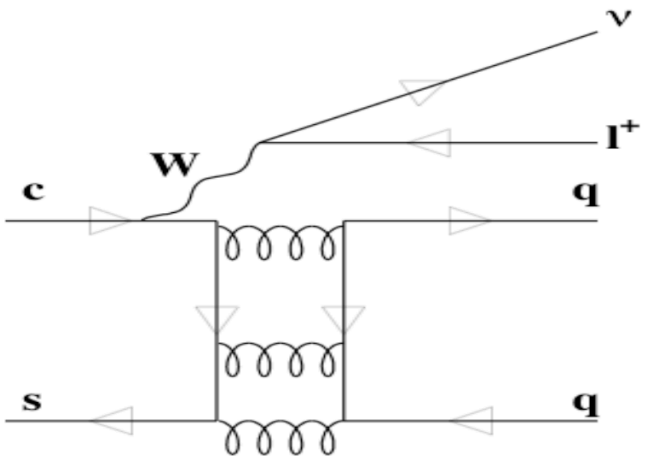

Figure 1.3: Semileptonic decay of the D_s meson through $\omega - \phi$ mixing.

Chapter 2: CLEO-c Experiment

High energy particles are not easily found in the universe. To study decays that are only observable at energies well above those found in nature's normal conditions, we must have a high energy source which would allow us to see what takes place. Particle accelerators and detectors play this role, and have evolved in interesting ways since the early 1930s.

The system of the accelerator CESR-c plus the detector CLEO-c studies primarily electron-positron annihilation events in the energy range 3-5 GeV

$$e^+e^- \rightarrow \gamma^* \rightarrow X.$$

By γ^* we indicate the virtual state, of mass equal to twice the beam energy, which rapidly decays into particles whose properties we seek to study.

2.1 CESR - The Cornell Electron Storage Ring

The Cornell Electron Storage Ring[35], or CESR, is an apparatus located at the Cornell University campus in Ithaca, N.Y. As shown in Fig. 2.1, CESR consists of three basic parts: a linear accelerator (linac), a synchrotron, and the storage ring. The storage ring and synchrotron are housed in a circular tunnel which has a diameter of 244 meters.The ring itself is roughly 12 m beneath the Alumni athletic field, with the CLEO-c detector collecting data from e^+e^- collisions in the south end of the tunnel. The linac is located in the inner part of the ring. The linac and synchrotron were built in the 1960's, with the capacity to accelerate electrons up to 12 GeV. The CESR storage ring was built in 1979 and was originally designed to run at center-of-mass energies up to 16 GeV, although it has operated at the Υ resonances (9.4-11.2 GeV)

until 2001.

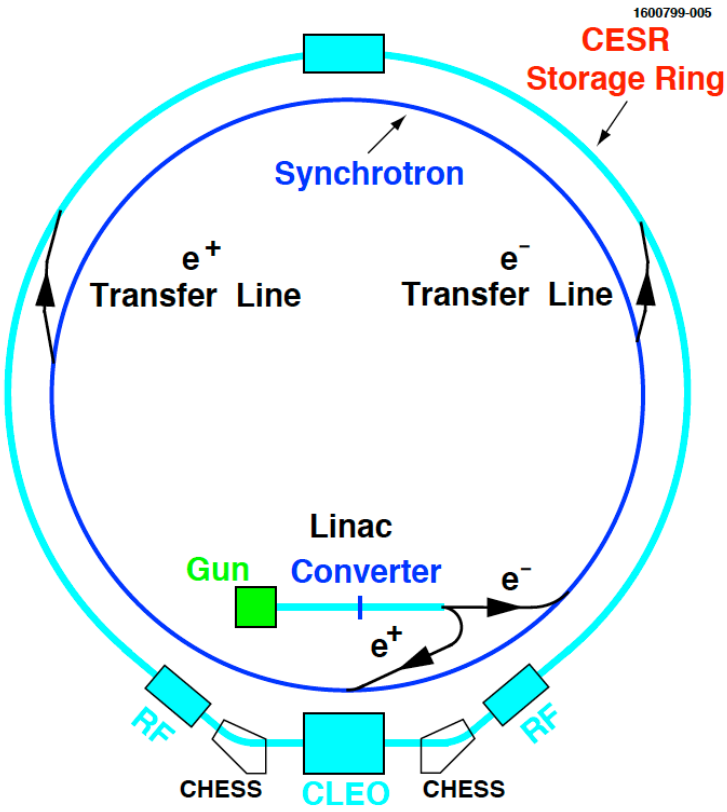

Figure 2.1: Image of CESR

The first CLEO detector was commissioned in 1979 to take advantage of the CESR storage ring to do B physics in the Υ region; the experiment's detector was upgraded in 1989 to CLEO II [36]and again in 1995 to CLEO II.V. The CLEO III detector, commissioned in 1999, was designed to keep the previous electromagnetic calorimeter (along with the muon chambers and magnet) and to replace all other parts, improving and refining the components from previous incarnations to achieve even better performance.

When it became apparent that the asymmetric B-factories would out-class CESR and CLEO in B production, the detector and accelerator were modified to run at charm-threshold energies (3-5 GeV) as CLEO-c and CESR-c. The CLEO-c detector[37] required only a modest modification of the CLEO III infrastructure, replacing the cen-

tral silicon strip detector with an additional wire tracking chamber and lowering the magnetic field strength in the tracking volume. CESR required the installation of wiggler magnets to provide additional beam instability damping. Synchrotron radiation, the usual mechanism for damping, is inadequate when running below the design energy. The storage ring and CLEO-c detector modifications, as well as the motivation and physics reach of the project, are fully described in the document "CLEO-c and CESR-c: A New Frontier of Weak and Strong Interactions" , with briefer descriptions following below.

2.2 CESR Accelerator and Storage Ring

The CESR linac (linear accelerator) is the source for electrons and positrons and accelerates those particles to an energy of 300 MeV before injecting them into the synchrotron; electrons and positrons are handled by the linac and the synchrotron at different times. Electrons are boiled off a filament and fired from a 150 keV electron gun into the linear accelerator. The linac consists of eight sections that use microwave cavities to accelerate the particles. Positrons are produced by diverting accelerated electrons to bombard a tungsten target; electromagnetic showers are generated by the collision, creating positrons via pair-production. The positrons are then collected, focused, and accelerated to 200 MeV. Afterwards, the particles are injected into the synchrotron, with positrons orbiting clockwise and electrons orbiting counterclockwise as viewed in Figure 2.1. In normal operation, positrons are injected first, followed by electrons.

The particles are accelerated in the synchrotron to the desired beam energy of about 2 GeV. There are 192 dipole magnets in the synchrotron for maintaining a roughly circular orbit, and four radio frequency (rf) acceleration cavities to provide the energy boost. The dipole magnetic fields are increased to maintain a stable orbit as the electrons or positrons gain energy. When the desired energy is reached,

the electrons or positrons are injected into the storage ring in "trains", or groups of bunches. CESR has the capability to operate with nine bunch trains, each train having up to five bunches, and 14 ns spacing between adjacent bunches. CESR currently operates with eight trains of four bunches for optimum beam conditions. The electron and positron bunches circle around the storage ring in opposite directions for the length of a "fill," or about one hour, which requires the beam conditions to be precisely maintained. The vacuum must be kept to less than 10^{-9} Torr to minimize losses due to beam-gas interactions. Along with dipole magnets to maintain the circular orbit, the storage ring has quadrupole and sextupole magnets to focus the beam. As the electron/positron beams circle in the storage ring, they lose energy due to synchrotron radiation; CESR uses superconducting niobium rf cavities to replace the radiated energy and maintain good beam conditions.

Because CESR is a single-ring, multi-bunch storage ring, the beams are maintained in so-called "pretzel orbits" to prevent the electron and positron beams from interacting except at the designated interaction region (IR). The number of crossing points is equal to twice the number of bunches, and so there are up to 89 crossing points which have to be avoided. Horizontal separators are used to give the beams antisymmetric orbit perturbations, preventing collisions at 88 potential crossing points, and a vertical separator prevents collisions at the crossing point opposite to the IR. At the IR, the beams have a small crossing angle of 2.5 mrads.

2.2.1 Luminosity and Changes for CESR-c

The most important measure of the performance of a storage ring is the luminosity it delivers. The instantaneous luminosity, L, can be loosely described as the rate at which particles are provided for collisions, independent of the interaction process. The instantaneous luminosity can be parameterized as

$$L = f\frac{n_1 n_2}{4\pi\sigma_x\sigma_y}. \tag{2.1}$$

where n_1 and n_2 are the number of particles in each of two colliding bunches, f is the frequency of bunch collision, and $\sigma_x(\sigma_y)$ is the Gaussian width of the particle distribution in the bunch in the horizontal (vertical) direction. Although the initial distribution of the particles in the bunch may not be Gaussian, the normal distribution is a reasonable model after reaching high energy [7].

The luminosity is important because it relates the number of observed events, N, to the invariant cross section σ for such event to happen,

$$N = L\sigma T,$$

where T is the time during which data is taken. High statistics studies, and the detection of ever rarer phenomena, can only advanced by producing high luminosity, as well as taking data for long periods of time.

2.3 CLEO-c Detector

When the CLEO Collaboration decided to focus on the lower energy charm sector, a few changes to the detector coincided with this shift in priority. One of these was the removal of the silicon vertex detector, which was replaced with an inner drift chamber, as vertexing would be less important under the new physics program. CLEO-c [37] consists of many layers of detector hardware, each with purposes that may overlap with those of other layers (See Fig. 2.2). It is housed in Wilson Laboratory at the south end of CESR, centered around the e^+e^- interaction region. The detector is almost entirely surrounded by a 1.0 Tesla magnetic field produced by a superconducting solenoid, which forces charged particles to follow a helical path. The magnetic field is along the CLEO's $z-$axis, which is the axis along which the beams

travel. Thus the magnet minimally bends the electron and positron beams, while it bends any particle that moves at a substantial cylindrical angle θ with respect to the $z-$axis.

Another interesting aspect of the conventions adopted in high energy physics is that the physical units are chosen so that $c = \hbar = 1$, so that mass, momentum, energy, and frequency all have the same dimensions, and spin values are pure numbers. The convention is adopted through the rest of this Thesis.

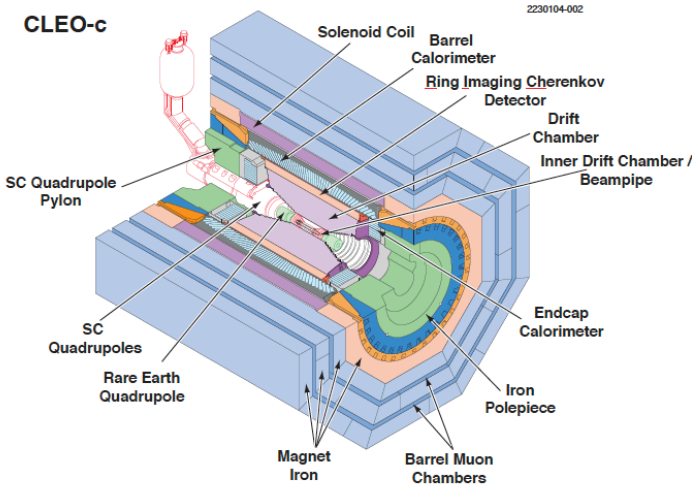

Figure 2.2: CLEO-c detector

The CLEO collaboration has a long history of focusing on excellent tracking, photon detection, and charged particle momentum resolution. The experience of twenty years with the detector and its upgrades has reduced systematic errors in tracking to 0.17%. The Cesium Iodide (CsI) crystal calorimeter is used to detect electromagnetic showers from electrons and photons and has almost the full 4π coverage of the solid angle around the interaction point. The superconducting solenoid that encloses the tracking chambers and calorimeter has a uniform and precisely measured magnetic field which helps to provide precise momentum measurements and particle identification via specific ionization (dE/dx). The Ring Imaging Cherenkov Detector (RICH)

also provides particle identification, separating kaons from pions.

2.3.1 ZD Replacing Silicon

The silicon vertex detector was designed for CLEO III to allow the measurement of vertices of D daughters of B decays and also to provide precise directional information on tracks. The device consisted of 4 layers of silicon strips, configured as double layers, with one side measuring z position and the other measuring r-ϕ . The position resolution was 24 microns in z and 11 microns in r-ϕ. For CLEO-c, however, the silicon vertex detector material would have significantly degraded the tracking through multiple scattering because the typical track momenta are lower than at CLEO III. Also, much of the motivation for the silicon detector is eliminated with the shift to running at lower energy. Since the CLEO-c D mesons are produced almost at rest, the flight paths would have been too small to be measured by the silicon detector's vertex reconstruction capabilities. For these reasons, a replacement detector for CLEO-c was needed between the beampipe and the main drift chamber.

A new cylindrical wire vertex chamber (ZD) was constructed for the CLEO-c detector, filling the space between radii 4.1 cm and 11.8 cm. The ZD was built from materials similar to those in the main drift chamber (described below), with gold-plated tungsten sense wires and gold-plated aluminum field wires. It has six layers of sense wires, held at 1900 V relative to the field wires, that are grouped into 300 cells. The ZD is designed to provide position information on charged particles within $\|cos\theta\| < 0.93$, where θ is defined with respect to the beam. The ends of the wires are displaced in the r-ϕ plane from one endplate to the other, giving a stereo angle (the angle between the endplates and the longitudinal center) that ranges from 10.5 degrees on the inside to 15.4 degrees on the exterior.

A signal is produced when a charged particle ionizes gas atoms in the drift chamber. The gas is 60% helium and 40% propane (C_3H_8); helium is chosen because of its

long radiation length (330 m), and the precise mixture optimizes position and energy resolution. The free electrons are accelerated by the potential towards the sense wire, ionizing other gas atoms and creating an avalanche. The electric charge (proportional to the energy deposited by the track) and the timing are recorded and contribute to track fitting by the main drift chamber. The z position resolution of the ZD wire vertex chamber is 680 microns, not nearly as good as the silicon vertex detector, but the momentum resolution is comparable on average to the silicon and even better at some energies.

2.3.2 Tracking Chamber

The outer, or main, drift chamber (DR) is a wire vertex chamber spanning from 12 to 82 cm in the radial direction. Along with the ZD vertex chamber, its purpose is to provide good particle identification, which is important for analyses of hadronic final states. There are forty-seven wire layers, with a total of 9796 of the gold-plated tungsten wires and 29,682 of the gold-plated aluminum field wires, grouped in open "cells". Each cell consists of eight field wires in a cage around one sense wire, with the sense wire held at high voltage relative to the field wires. Of the forty-seven layers, the first sixteen are all axial and the remainder alternate stereo angles of about 3 degrees in groups of four. The sense wires are held at a potential of 2100 V relative to the field wires. The gas inside the main drift chamber is the same as in the ZD, a 60:40 mix of helium and propane. The inner surface of the exterior shell is segmented into cathode strips which provide z position information on tracks.

Like the ZD vertex chamber, the main drift chamber provides position and energy loss information when a charged particle ionizes gas in the drift chamber as it passes through. A track is reconstructed based on the wire hits from both drift chambers using pattern recognition software. A fitted track yields momentum information based on the curvature of the trajectory in the magnetic field from the solenoid. The drift

chamber has position resolution of 85 microns and momentum resolution from this fit of σ_p/p of 0.35% at 1 GeV/c.

The rate of energy loss (energy deposited per unit length or dE/dx) is compared to theoretical values for different particles to make an hypothesis as to particle identity. The deviation from the particle-hypothesis for a single measurement variable is defined as follows:

$$\chi_i = \frac{dE/dx(measured) - dE/dx(expected)}{\sigma_i} \tag{2.2}$$

where σ_i is the uncertainty on the measurement, usually about 6%. An overall χ^2 is formed for each particle identity hypothesis of electron, muon, pion, kaon, or proton by summing the χ_i^2 over many hits. The value of $dE/dx(measured)$ is plotted against particle momentum for each charged particle in Figure 2.3.

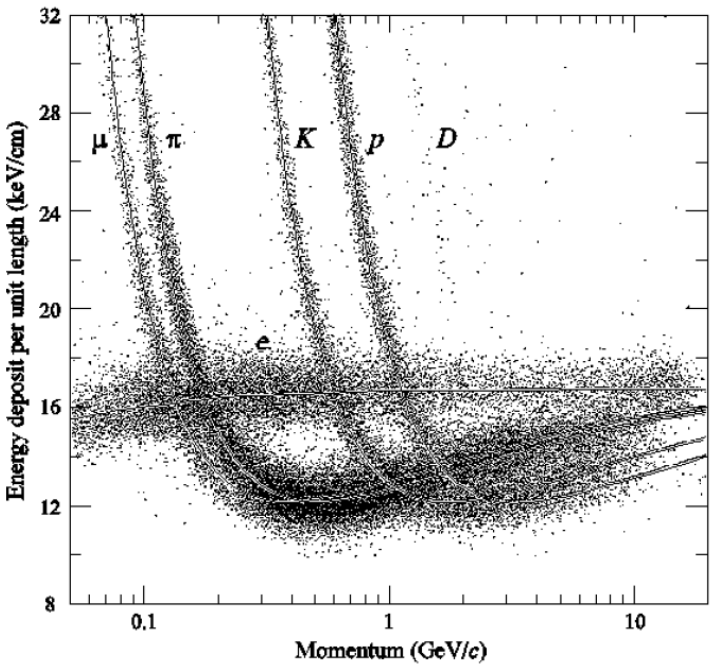

Figure 2.3: dE/dx scatter plot as a function of track momentum. The various bands are labeled to show which particle produced them.

Fig 2.4 shows the separation between pions and kaons (the majority of charged

hadronic particles in CLEO-c) in dE/dx over the typical momentum range in CLEO-c. Separation is greater than 5σ below 600MeV/c and is still greater than 3σ at 700MeV/c. At higher momenta, additional information is needed for good particle identification.

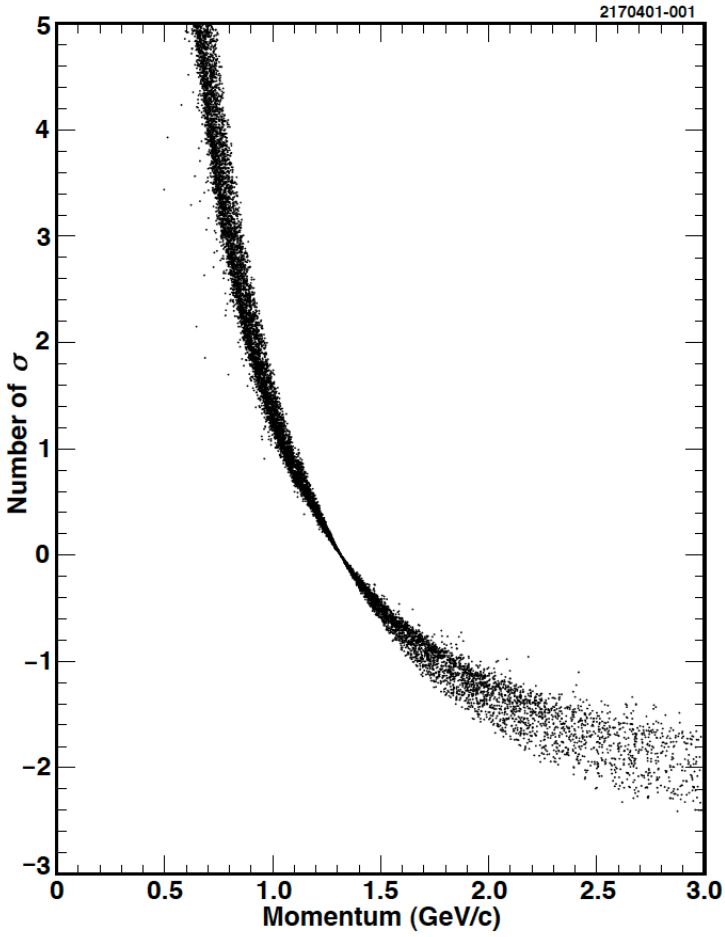

Figure 2.4: Statistical separation of kaon and pion candidate tracks with dE/dx

2.3.3 RICH Detector

The RICH detector[38] uses Cherenkov photons to provide particle identification over 83% of the 4π solid angle. Cherenkov radiation is produced by the constructive interference of EM waves emitted when a charged particle moves faster than the local speed of light in a dielectric medium. The charged particle polarizes nearby atoms,

which release UV photons to return to their ground state. The wavefronts produced by the constructive interference are conical, centered on the particle trajectory, and have a characteristic angle that is related to the velocity of the particle:

$$cos\theta_c = \frac{1}{n\beta}, \tag{2.3}$$

where β is the velocity relative to c and n is the index of refraction for the dielectric medium. If there is independent knowledge of the particle's momentum then a calculation can be made of the particle's mass from the opening angle of the Cherenkov light:

$$\beta = p/E, E^2 = m^2 + p^2, cos\theta_c = \frac{1}{n}\sqrt{(}1 + \frac{m^2}{p^2}), \tag{2.4}$$

allowing a likelihood to be constructed for the particle's identity.

LiF crystals were used as the dielectric medium to generate Cherenkov photons; although expensive, their low-Z value minimizes the likelihood of an electromagnetic interaction with photons from one of the decay products. There are fourteen rows of crystals, with the rows at the center of the barrel having sawtooth surfaces to prevent total internal reflection, and rows near the edge of the barrel are smooth. UV photons exit the LiF crystals into the N_2 expansion volume, where the cone of Cherenkov photons widens. These photons then pass through CaF_2 windows into a methane-TEA (triethylamine) gas, where the UV light produces photoelectrons which are collected at cathode pads and converted to signal.

To use RICH information for particle identification, a χ^2 variable difference was constructed based on likelihood variables, taking into account different light paths produced by difierent particle hypotheses:

$$\chi_i^2 - \chi_j^2 = -2ln(L_i) + 2ln(L_j), \tag{2.5}$$

where i, j can be electrons, muons, pions, kaons, and protons. Fig. 2.5 shows the separation of particles with CLEO-c RICH detector. The dotted line cuts off at the minimum for both particles hypotheses to emit Cherenkov photons in LiF radiator.

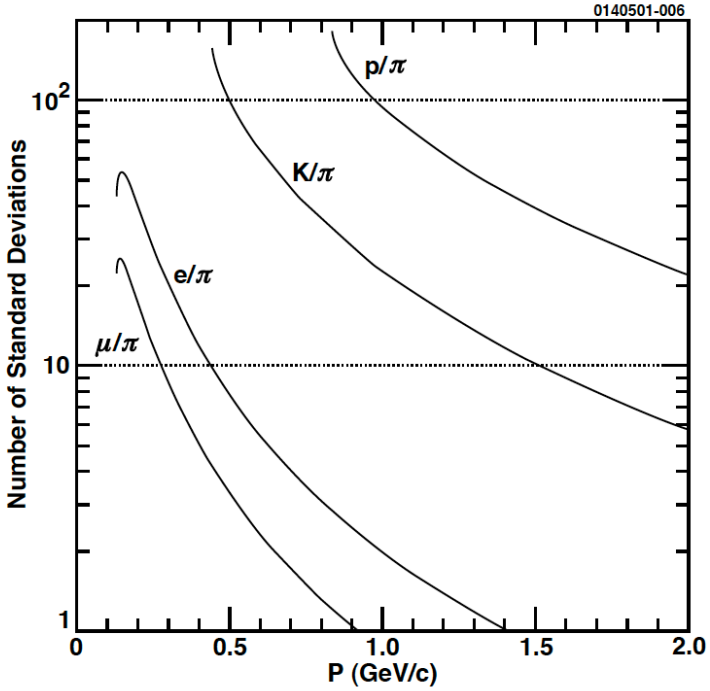

Figure 2.5: Theoretical separation of particles with CLEO-c RICH detector by momentum. The dotted line cuts off at the minimum for both particles hypotheses to emit Cherenkov photons in LiF radiator.

For K and π separation, a typical selection requirement of $\chi^2_K - \chi^2_\pi < 0$ identifies 92% of kaons with only an 8% fake rate for pions (Fig. 2.6).

2.3.4 CsI Calorimeter

The electromagnetic calorimeter measures the energy deposited by particles through ionization, Brehmsstrahlung, pair production, or nuclear interactions, and is the only way for CLEO-c to detect neutral particles. Good calorimetry is necessary to have clean signals for modes with π^0's and to keep photon backgrounds low. The calorimeter is located between the RICH detector and the superconducting solenoid and has 93% of 4π coverage (shown in Fig. 2.7).

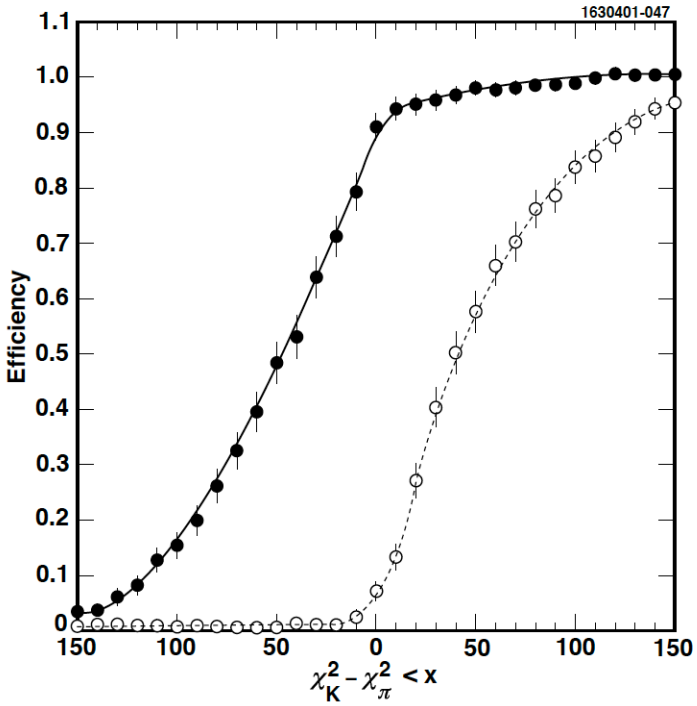

Figure 2.6: Kaon efficiency (filled circles) and pion fake rate (open circles) as a function of χ^2 diffference between kaon and pion hypotheses for the CLEO-c RICH detector. Tracks included are measured to have momentum between 0.7 and 2.7 GeV/c.

It consists of about 7800 thallium doped CsI crystals (5 cm x 5 cm x 30 cm, see Fig 2.8), each of which is triple wrapped with 0.04 mm thickness white teflon and once with 0.01 mm aluminized mylar to keep photons from escaping the crystal. About 80% of the crystals lie in the barrel region, covering $|cos\theta| < 0.8$, and project radially away from the beamline. The two endcap regions cover $0.80 < |cos\theta| < 0.93$ and have crystals extending parallel to the beamline. The energy resolution and efficiency for the end-cap region is slightly worse than for the barrel because of additional intervening material. The transition region between barrel and endcap, from $0.80 < |cos\theta| < 0.85$, does not have as good resolution as the rest of the calorimeter due to the additional material at that angle and crystals in this region are commonly not used. Fig.2.9 shows the diffference in signal to background and resolution for π^0 mass with two versus only one shower in the barrel region.

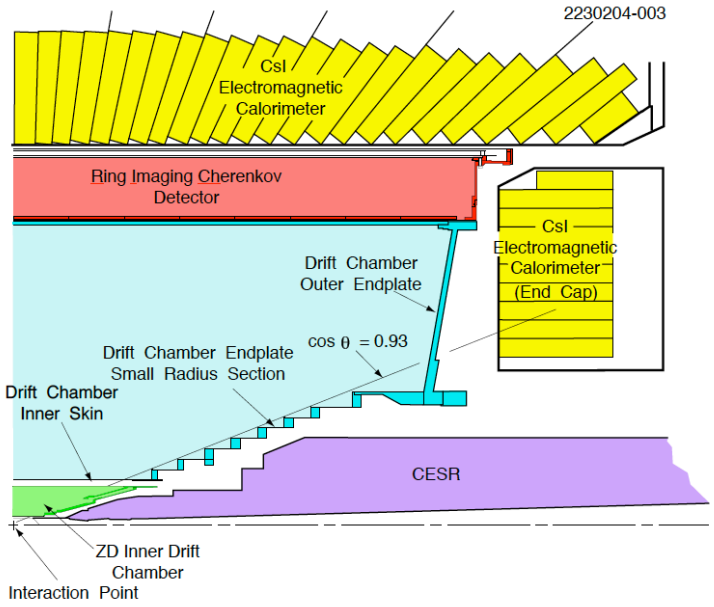

Figure 2.7: CLEO-c detector cross-section image showing CsI Calorimeter and other detectors.

The signals from multiple crystals registering energy deposition must be combined to detect all of the energy of photons or electrons. All crystals recording a signal are combined into a cluster, with the requirement that each is at most two segments away from another crystal in the cluster. The most energetic crystal in the cluster is defined to be the crystal with energy above 10 MeV and recording higher energy than any of its adjacent neighbors. The energy of the cluster is calculated based on the N most energetic crystals in a cluster; N varies logarithmically with energy, ranging from 4 at 25 MeV to 17 at 4 GeV. This algorithm improves energy resolution over using all crystals in a cluster, as the lowest energy crystals are dominated by noise. When a crystal is used by more than one cluster, the energy is considered to be split among the clusters. The centroid of the cluster is found by summing the energy-weighted coordinates of the crystals used in shower reconstruction, and the shower position is this centroid plus a small correction accounting for the geometry of the detector. The crystals' energy response is calibrated using Bhabha-scattering events, $e^+e^- \to e^+e^-$.

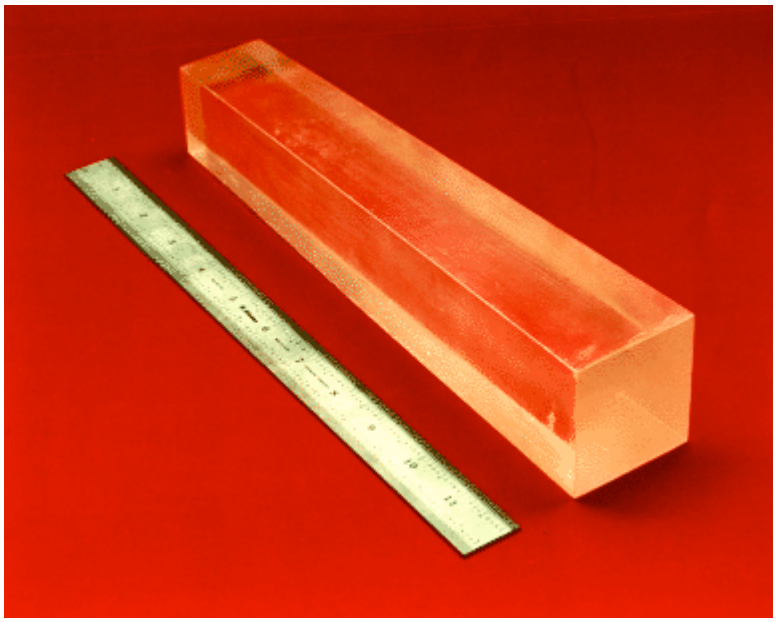

Figure 2.8: CLEO-c CsI crystals.

The CLEO-c calorimeter has angular resolution of 10 mrad and energy resolution of 4.0% at 100 MeV and 7% at 30 MeV.

Electrons and photons deposit energy through electromagenetic showers, with a high rate of energy loss due to high-Z nuclei. At typical CLEO-c energies, photons undergo pair conversions to electrons and positrons, while electrons primarily lose energy through Bremsstrahlung. The end products, low energy electrons, deposit energy via ionization, exciting atoms in the CsI(Th) crystal which emit visible light (560 nm photons) to return to their ground state. The crystals are transparent at this wavelength, and the 560 nm photons produced by deexcitation are collected at the end of the crystal by four 1cm x 1cm PIN photodiodes.

Hadrons lose energy electromagnetically at slower rates in the calorimeter due to the higher mass, but can also deposit energy through strong interactions with nuclei. One result is the creation of neutral pions decaying to photons, which then follow the energy deposition process outlined above. However, the CLEO-c calorimeter does not have sufficient material to capture enough of an hadronic shower to make a useful energy measurement. Muons are minimum ionizing particles and escape the

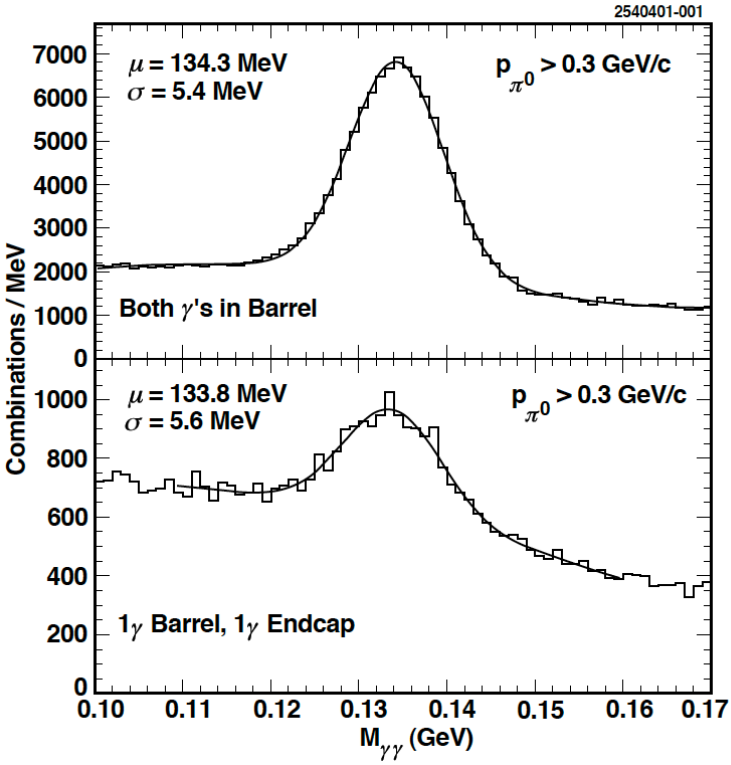

Figure 2.9: π^0 resolution from CLEO III data for candidates with both photons in the barrel region (top) and with one photon in the barrel and one in an end cap (bottom).

calorimeter into the muon chambers.

In summary, the energy and angular resolutions for barrel showers were 3.8% and 11 mrad at 100 MeV, and 1.5% and 3 mrad at 4 GeV.

2.3.5 Muon Chambers

There is also a muon detector surrounding the other CLEO-c components, consisting of interleaved wire chambers and layers of iron. The iron screens out other particles, meaning that hits seen in the wire chambers can only be due to muons. However, the muon detectors are not used for most CLEO-c analyses because the acceptance of the system is poor at the momentum range of muons produced at center-of-mass 4 GeV , because the detector was designed for 1 GeV and higher

muons.

2.3.6 Magnets

The CLEO III detector's superconducting solenoid produced a field of 1.5 T within the detector. While this was superior for running at center-of-mass energies around 10 GeV, with average charged particle momentum of 530 MeV/c, charm threshold energies produce tracks with a lower average momentum of 395 MeV/c and a significant number of low momentum tracks. Lowering the magnetic field to 1.0 T in CLEO-c has two main benefits for low momentum tracks. First, low momentum tracks (60-80 MeV/c) will penetrate deeper into the drift chamber, producing more hits and raising the detection efficiency. Second, it will reduce the number of "curlers", or tracks that are associated with low-momentum particles that have trajectories with diameters smaller than the radius of the main drift chamber. At 1.5 T, these are particles with transverse momenta less than 180 MeV/c. Curlers present a challenge because the pattern recognition is impaired for the entire event. A reduced solenoidal field produces a greater radius of curvature, allowing the low momentum particles to escape the drift chamber. CLEO-c runs with a 1.0 T magnetic field, uniform to within $\pm 0.02\%$.

2.4 Data Acquisition and Triggers

CLEO-c employs a trigger system to maximize the efficiency for collecting events containing interesting physics while minimizing the amount of extraneous signal. While maximum efficiency would be achieved by digitizing every signal recorded by the detector, the data acquisition system (DAQ) has limitations on the rate of moving data to an archive. The time between receiving the trigger signal and the end of the digitization process is called "dead time" because any event occurring during that time is lost. Since some events will be lost, it makes sense to spend time recording

useful events and to drop uninteresting ones, which is handled by predefined triggers. The trigger lines are developed according to the specifications of the DAQ, to deliver events that meet certain criteria as physics of interest while minimizing dead time.

2.4.1 Data Acquisition System

The performance of the DAQ is determined by its ability to minimize dead time by quickly moving signal from components to storage media; the performance of the CLEO III DAQ includes data read-out rate and data transfer bandwidth.

The data transfer bandwidth depends on the event size (average of 25 kBytes) and the read-out rate can be calculated from the total cross-section, the luminosity, and the trigger efficiency. The upper bound on the luminosity assumed in designing the DAQ was $5 \times 10^{32} cm^{-2} s^{-1}$, while the cross-section at the $\psi(3770)$ energy was estimated to be 560nb. Bhabha scattering makes up 500nb of that cross-section. with the remainder coming from charmed particles, continuum processes, and $\tau^+\tau^-$ pairs. The rate of Bhabha events is reduced by an adjustable prescaling factor, down to a more manageable effective cross-section of 160 nb. For a trigger efficiency of 100%, the read-out rate based on the effective cross-section is 80 Hz; with an event size of 25 kBytes, the bandwidth needed is 2.0 MBytes/s. An average read out time of 20-30 μs per event with this read-out rate yields an average dead time of less than 0.3%. Based on these numbers, it was judged that the CLEO III DAQ is sufficient to handle the environment at CLEO-c. In practice, with smaller-than-expected luminosity, the performance has been excellent.

The structure of the CLEO III DAQ is diagrammed in Figure 2.10, showing the flow of data from the data board buffer of each CLEO III detector component (a total of 400,000 detector channels) to the final record; the CLEO-c DAQ differs in the replacement of the Si-VERTEX component with the ZD wire chamber. Electronics local to each component hold data in buffers; the DAQ is activated when a trigger line

approves the buffered signal. The signal is then transferred through the component's Data Mover. This transfer to Level 3, the final trigger stage, is done in 500 μs or less. Here, beam-gas and beam-wall interactions are selected out. Finally, the Event-Builder receives the data from all the detector channels, constructs an event, and records it to disk. All this occurs only if a trigger line indicates that the event matches criteria for a particular kind of physics. CLEO-c currently uses eight triggers (out of 24 available in the hardware) with variable prescaling, as shown in Fig 2.11 with the relative rates after prescaling.

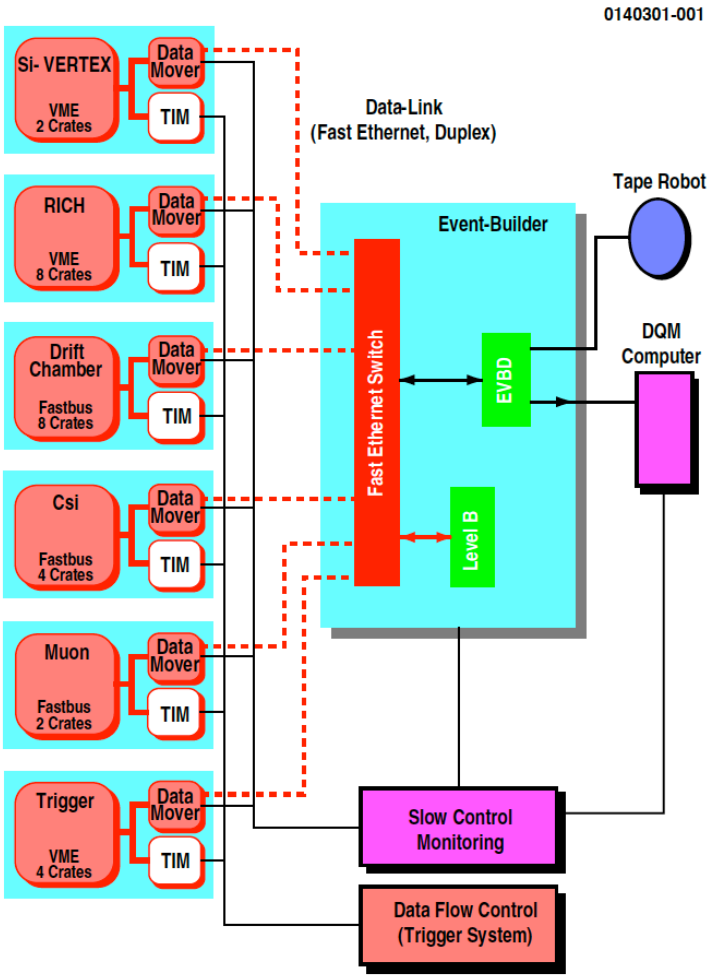

Figure 2.10: DAQ flowchart from CLEO III.

If an event is passed, a Level 1 pass signal is sent and the information is moved

trigger line	definition	relative rate
Hadronic	$N_{axial} > 1$ & $N_{CB\,low} > 0$	0.41
$\mu - pair$	back-to-back stereo tracks	1.40
barrel Bhabhas	back-to-back high showers in CB	1.0
endcap Bhabhas	back-to-back high showers in CE	0.23
electron+track	$N_{axial} > 0$ & $N_{CB\,med} > 0$	1.48
τ/radiative	$N_{stereo} > 1$ & $N_{CB\,low} > 0$	2
two track	$N_{axial} > 1$	0.69
random	random 1 kHz source	1

Figure 2.11: CLEO triggers

to storage by the DAQ; otherwise, the information can be dropped to allow the next signal to be captured. Data from each component is processed in a separate VME crate to produce basic trigger primitives (track and shower counts, and the topologies of each) for use by the two hardware trigger systems. Both hardware triggers and the global trigger use MVME2304 Power PC modules to act as crate controllers (CTL) and data movers (DM). Also, there are trigger interface modules (TIM) to regulate clock signals and send "pass" or "busy" signals.

The total trigger rate for $L = 5 \times 10^{32} cm^{-2} s^{-1}$ is between 40 and 45 Hz. The hadronic trigger is the primary source of data for this analysis, with the trigger on Bhabhas providing information on the luminosity. The instantaneous luminosity is calculated using information from the Bhabha trigger to estimate the rate of Bhabha events and reported to the CESR control room.

2.5 Summary of CLEO-c resolution and efficiency.

The ultimate figures of merit for a multi-purpose detector such as CLEO-c are the resolutions and efficiencies for each distinct particle which we seek to detect. These were given in the Subsections devoted to each detector.

The detector resolution enters in the determination of each kinematic quantity we compute in the analysis. In the simplest example, the invariant mass squared, M^2, of two photon-like objects, is computed as $M^2 = 2E_1E_2(1 - cos\theta)$, where the E_i are

the energies reconstructed in each object, and θ is the angle obtained using the IP as the angle vertex, and the two vectors pointing from the IP to the geometric center of each object.

Assuming fractional and energy-dependent energy resolutions ϵ_1 and ϵ_2, and energy-dependent angular resolutions δ_1 and δ_2, the M^2 fractional resolution reads as $\sigma^2 = \Sigma(\epsilon_i)^2 + \frac{sin^2\theta}{(1-cos\theta)^2}\delta_i^2$.

The $\pi^0 \rightarrow 2\gamma$ mass spectrum, then, looks like the one in Fig. 2.9. These are the π^0 objects we use in the analysis described in Chapters 3 and 4.

The efficiency is defined as the fraction of reconstructed particles compared to all the particles that were generated at the interaction point. Because the angle around the beam pipe can not be instrumented, low angle particles of all types will always be lost. Other effects that diminish the efficiency are decay in flight, multiple scattering in the beam pipe and detector structure, and very low momentum for tracks. For photons, very low energy, conversion in the beam pipe and detector structure, photon overlap with other photon and non-photon showers, all contribute to efficiency losses.

In our analysis described below, our signal is made with three tracks and two photons, so that our efficiency is proportional to $\epsilon_t^3\epsilon_p^2$. Further selection cuts we use, to define a candidate electron, further reduce the efficiency. Minor corrections are also due to particle correlations, and the fact that selection cuts inevitably cut some good tracks.

2.5.1 Data sets and analysis software.

The collaboration has developed a very mature set of software libraries, written in C++, that are used to turn the raw readout information into physics "objects" that physicists can use in analyses. This is done after the triggering and data acquisition, on a timescale not necessarily related to the operation of the detector. Collaboration members then write analysis code, mostly in C++ with other languages and shells

used to supplement, that ask questions such as: "Is there a $D^0 \to K^-\pi^+$ decay in this set of events?" If a member is interested in more details, the raw readout information is also available for query.

The bulk of the data reconstruction is done with software called "pass2," which contains tracks and showers, and some initial object identification. The analysis presented here uses data that has been further processed into a "D Skim," in which the objects built in pass2 are combined in ways to make D meson candidates. It is important to remember that pass2 does work on the entire event, including secondary decays that occur as the primary decay daughters enter the detector. The D Skim, as the name implies, skims the pass2 events to reduce the data set a physicist has to look at, but using minimal quality cuts that lose little or none of the interesting events. If a D candidate is identified by D Skim, the rest of the event is still potentially important and is saved for further analysis. The D Skim will be discussed further in Chapter 3.

2.6 Monte Carlo

An important software application is the generation of simulated Monte Carlo data (MC) [29] that is used to test analysis techniques. The simulation takes place in two parts: first, software called EvtGen simulates the decay of the $\gamma^\star$ down to final products; second, detailed simulations of how the various detector components respond produce mock detector output. One can apply analysis code to MC the same way as data, going through the analysis and not looking at anything simulation specific.

The real power of MC, however, is that one can look into the EvtGen decay tree and see exactly what was produced and how it interacted with the detector. This is useful for investigating how signal can be faked and how often a real signal is properly found by the analysis code. Identification of a strong background source can provide

clues of how the selection cuts should be improved to reduce background.

Of course, there are differences between MC and data, because EvtGen does not know everything about nature (most notably, the properties of low-energy QCD can not be computed precisely), and because the detector is not perfectly simulated.

The collaboration produces what is called "generic MC," which is a simulation restricted to $(D^0\bar{D}^0)$ and (D^+D^-) pairs. This is also D Skimmed, so an analysis may easily use D tags in both MC and data. There is also a set that mimics non-$(D\bar{D})$ events called "continuum MC". This is important because there are as many or more continuum events in data as there are $(D\bar{D})$. The generic Monte Carlo discussed in the next Chapters always includes both of these events.

Other types of MC exist, and custom MC can be produced if one requires extra features not available in the collaboration-wide MC sets. Below, we produce results from several dedicated Monte Carlos, which allow us to study detailed properties of our events in greater detail. MC is always linked to a dataset, so it can be calibrated to match CESR and CLEO conditions during that dataset.

2.7 Software

It is useful to understand the software tools and sequence of analysis tasks used to make yield measurements and perform fits. For the purposes of this discussion, text that refers directly to words in software code, scripts, or command line entries are presented in *italic*. Shell commands are prefixed with the shell prompt character $.

CLEO-c analysis tools and libraries operate primarily on computers running the GNU/Linux operating system, with some legacy support for proprietary UNIX operating systems. Source code for the main C++ analysis libraries is fully available and searchable through a web interface, and generally good documentation lives online and in documents internal to the collaboration called CBX notes. These software

libraries provide a vast number of C++ objects and functions that are used to access the MC and data. There are also a number of utilities and scripts used to make life easier for collaboration members. One utility, *mkproc*, allows one to start a new analysis package very easily. The working skeleton of an analysis intended to run on D Skimmed data and MC can be produced with the command *mkproc ProcessorName -dtag* that builds a directory of C++ files (including *ProcessorName.cc* and *ProcessorName.h* files) with example code that is ready to compile. The task of the experimentalist is to modify this new "processor" for his specific analysis. This code is compiled using the *make* command, which in turn calls the GNU Compiler Collection C++ compiler, g++. The Makefile that directs the compilation is included with the *mkproc* output.

Upon compilation, a binary shared object is produced, with a name of the form *ProcessorName_software_version.so*. This file is not directly executable. The code is run within a framework called *suez*, which handles the availability of data/MC and loads other shared objects necessary for the analysis. *suez* is controlled by scripts written in the Tcl scripting language, in which one sets the proper environment variables, loads other shared objects, defines the data ranges to investigate, and references the main analysis code. For small test jobs, *suez* can be run on a desktop workstation, but for full-fledged analyses, *suez* is run on a computing farm reserved for this purpose. Jobs are submitted to the farm via the Grid Engine queueing system, which manages how computing resources are available to experimenters. The qsub, qdel, and qstat commands allow for submission to, removal from, and display of jobs in Grid Engine.

Output is provided in two ways. Log files, containing messages from *suez* and from the analysis code itself, are defined in the Tcl scripts. These are useful for diagnosing bugs and errors, and are the most useful mechanism for investigating MC truth information. Separately, files are defined by Tcl scripts that serve as

the repository for experimental information distilled by the analysis code. These repositories are in the form of HBOOK files, with the extension .rzn. HBOOK is a histogram software library developed at CERN. These files contain histograms and multi-dimensional data structures called "ntuples". An ntuple is used to store many items of information from a single event, such that the items are logically linked. It is then possible to take a set of events stored in ntuples, make a cut on one of the variables stored in the ntuple, and have a resulting set of events that pass this cut, with the rest of the stored event information still intact. In this way, a series of analysis steps can be performed on ntuples external to the operation of the main C++ analysis code.

Whether certain analysis steps are performed in the C++ code or afterward by operating on the HBOOK files is largely a matter of preference. The C++ code generally takes much longer to run than ntuple manipulation, as long as the ntuples are small enough. The basic strategy tends to use the C++ libraries to directly access data/MC, eliminate obvious backgrounds, investigate MC, and fill manageably-sized ntuples with information about each event that passes basic selection cuts. After this, separate software packages such as *root, mn fit*, or custom Fortran binaries are used to make further cuts and produce plots of important variables.

While *root*, a powerful and modern data analysis package, is arguably the current popular tool of choice, this analysis uses a combination of Fortran binaries and *mn fit* for ntuple manipulation. The software written in Fortran looks at ntuples, makes cuts, and outputs one-dimensional histograms. These histograms are then used by *mn fit*, a plotting and fitting package, for final analysis touches, fitting and display. *mn fit* has a unique command language, and can be used interactively or via prepared scripts. Plots are generally output in the PostScript format.

2.8 Previous Results

Since its inception, the CLEO Collaboration has published hundreds of articles, many of high importance to the field. Measurements of B mesons to final states with no charm quarks are sensitive to the CKM matrix element $\|V_{ub}\|$, and CLEO discovered numerous forms of these decays [31]. CLEO discovered many charmed baryon decay modes, and measured meson decay constants f_{Ds} and f_{D^+}. CLEO has published papers on the properties of quarkonia , which are bound states of a quark and its antiquark. It has also made discoveries of decay modes of the tau lepton, and performed searches for particles predicted by theories beyond the Standard Model.

Chapter 3: Experimental Method

3.1 Overview

In this Chapter the methods of selection of interesting events are described. Because we do not distinguish between the D_s and its anti-particle, both in the following are generically indicated as D_s.

Our experiment uses the data collected in e^+e^- interactions at $\sqrt{s} = 4170$ MeV. At this energy, 95% of the electron positron collision resulting in at least one D_s meson (the inclusive process $e^+e^- \to D_sX$) are in fact the exclusive process $e^+e^- \to D_sD_s^*$[39]. About 95% of the D_s^* will decay through the channel $D_s^* \to D_s\gamma$. In total, about 90% of all events containing a D_s come from the exclusive reaction $e^+e^- \to D_sD_s\gamma$.

This interesting fact allows a deep reduction of backgrounds. The cross-section for the channel of interest is roughly 1 nb. Other charm production totals about 7 nb [39], the underlying light-quark "continuum" is about 12 nb, and the τ lepton cross section is about 4 nb. However, by requiring a well-reconstructed event, a total of four kinematic constraints can be applied, which ultimately give a sensitivity to the branching ratio $D_s \to \omega e\nu$ of order 0.1%.

The experimental method consists of searching for ω candidates through its dominant decay mode ($B(\pi^+\pi^-\pi^0) = 89.2\%$). Cabibbo favored decays exist in the same final state, $D_s \to \eta e\nu$ and $D_s \to \phi e\nu$, the two hadrons having respectively $B(\pi^+\pi^-\pi^0)$ of 22.73% and 15.32% [14]. They can play the role of control samples, which are used directly in the analysis in a variety of ways. For example, the effect of certain selection cuts can be readily estimated from any change in the η and ϕ populations. We have also used the information from our η and ϕ samples to cross check against the

data set	$\sqrt{s}$ (MeV)	$L(pb^{-1})$
39	4170	55.049
40	4170	123.960
41	4170	119.126
47	4170	109.795
48	4170	178.269
total		586.199

Table 3.1: Summary of data used in this analysis

parallel Rochester analysis, and to cross check the strongly correlated fit results using double Gaussians.

The two control samples are also well measured using the independent final states $\eta \to \gamma\gamma$ and $\phi \to K^+K^-$. Therefore, this analysis has good statistical sensitivity, due to the favorable ratio of branching ratios ($89/23 = 4$), and unusually strong control samples using CLEO-c data directly.

The search of $D_s \to \omega e\nu$ decay contains two parts. The decay is certainly rare, so that the possibility of both particles decaying this way can be neglected. The event is then divided in two parts, the "signal", containing the ω and the electron, and the tag, which contains the other D_s and the γ and can be reconstructed and used for background rejection purposes.

The two control samples $\eta e\nu$ and $\phi e\nu$ are also well measured using the independent final states $\eta \to \gamma\gamma$ and $\phi \to K^+K^-$. Therefore, this analysis has good statistical sensitivity, due to the favorable ratio of branching ratios ($89/23 = 4$), and unusually strong control samples using CLEO-c data directly.

3.2 Data Samples

We used $586pb^{-1}$ of data produced in e^+e^- collisions at CESR near the center-of-mass $\sqrt{s} = 4170$ MeV. Data sets used in this analysis are summarized in Table 3.1, we processed v2 D-skim over data 39, 40, 41, 47 and 48.

The detector response is modeled with a detailed GEANT-based Monte Carlo

(MC) simulation, with initial particle trajectories generated by EvtGen and final state radiation produced by PHOTOS. The initial-state radiation is modeled using cross sections for $D_s^* D_s$ production at lower energies obtained from the CLEO-c energy scan near the CM energy where we collect the sample. We have two sources of MC events: the Generic Monte Carlo (GENMC), which contains all charmed particle events, with 20 times the number of events in the data, and the continuum MC, containing 6.6 times the number of events in the data.

3.3 Object reconstruction.

Before tags and signal can be reconstructed, each of the charged and neutral particles need to be identified and their 4-momentum measured.

3.3.1 Track selection and efficiency

The detection of charged particles has been important to nuclear and particle physics since the invention of the cloud chamber by Nobel Prize winner Charles T. R. Wilson in 1911. A charged particle traveling through a magnetic field is deflected, and in CLEO the magnetic field is very close to constant and parallel to the beampipe. The curvature that these particles experience provides a way to measure their momentum, as long as the path can be identified.

As explained in chapter 2, we utilize two particle identification (PID) devices to separate charged kaons from pions: the central drift chamber, which provides measurements of ionization energy loss (dE/dx), and, surrounding this drift chamber, a cylindrical ring-imaging Cherenkov (RICH) detector, whose active solid angle is 80% of 4π.

Tracks used in the reconstruction of signal must pass a set of selection cuts, most of which are listed as follows:

1. TRKMAN ok. This package rejects fake tracks from loopers.

2. Track fit ok and not fit abort. The software successfully performed the fit.

3. $\chi^2 < 100000$. The residual of a hit is the distance between measured hit and fitted track, divided by the exepected resolution. The sum of all residuals, squared, is the χ^2 and is low for a good quality fit.

4. Hit fraction ≥ 0.5. At least 50% of the cells crossed by the fitted track must have a hit associated with the track.

5. Distance of the fitted track to the interaction vertex in the bending plane $|d_0| \leq$ 5 mm.

6. Distance of the fitted track to the interaction vertex in the non-bending plane $Z_0 \leq 5$ mm.

7. $|cos\theta| < 0.93$

8. Track momentum: $0.05 \leq p_{track} \leq 2.0$ GeV.

The selection cuts are designed to find kaons and pions that have produced good quality tracks and have originated from a spot close to the interaction point. (Recall that the D mesons produced at CLEO-c have low kinetic energy, and do not travel far before decaying.) The usage of good quality tracks is necessary for virtually any analysis, since the data are analyzed much further before extracting the final result, and even a single poor quality track in the event affects virtually every step of the final analysis.

Efforts are also made to differentiate kaons and pions, using the dE/dx and $RICH$ info described above. A combined log-likelihood is calculated from dE/dx information (denoted σ_π and σ_K) and $RICH$ output (denoted L_π and L_K). In the case of pions, the quantity

$$L = \sigma_K^2 - \sigma_\pi^2 + L_K - L_\pi \tag{3.1}$$

must be positive. If the track has momentum $p < 0.70\text{GeV}$, $|\cos\theta| > 0.8$, or if the RICH detector has produced obviously wrong output, then L_π and L_K are omitted. The momentum and $\cos\theta$ cuts deal with RICH limitations. If we want to identify kaons, Eq. 3.1 is also used, except with subscripts π and K swapped.

The study of high-momentum muons in Ref. [40] shows efficiency of nearly 100% in both data and Monte Carlo. Pions, on the other hand, show some inefficiency. The crucial difference is that muons almost never decay or interact inside the detector, but pions sometimes do. The muon efficiency measurements suggest that when a track passes through the entire drift chamber, the efficiency for reconstructing it is nearly 100%. The only way a track can be lost is if it decays or interacts inside the DR[40].

The combined PID system has a pion or kaon efficiency $> 85\%$ and a probability of pions faking kaons (or vice versa) $< 5\%$. 0.3% systematic uncertainty was suggested[40] for each pion or kaon track, combined in quadrature with a 0.6% systematic for each kaon.

3.3.2 Electron selection

As mentioned in previous chapter, electrons deposit most of their energies in the CsI crystals. Therefore, neglecting the small electron mass, the ratio of the energy measured in the calorimeter to the momentum measured in the tracking chambers should be near one for electrons. Heavier particles, which do not initiate electromagnetic showers, should have E/p values less than one.

The identification of electrons is very important, as semileptonic decays play a vital role in this analysis. The electron ID (EID) package used in CLEO-c was developed by C. S. Park under the guidance of E. Thorndike[41]. It looks at tracks in events with a D tag that are not included in the tag reconstruction, and that pass a set of quality cuts, and sets the variables F, Fveto, and Fw/R. These variables range from zero to one and indicate how much the track looks like an electron. The first

just uses dE/dx information, the second uses RICH output to veto candidates that are probably not electrons, and the third fully incorporates RICH information. A standard EID cut is to require that a track has $F_{w/R} > 0.8$ to be called an electron. Unless otherwise specified, this is how electrons are identified within this analysis.

3.3.3 Photons.

As explained in chapter 2, the energy of electrons and photons is determined by cesium iodide crystals. The electrons and photons enter the crystals and initiate a cascade of photons, which travel to the far end of the crystal and are detected by silicon photodiodes. The total intensity of light is proportional to the energy of the incoming object.

Showers were reconstructed by first converting the amount of light detected in each crystal into a deposited-energy estimation. Since showers frequently spanned multiple crystals, clusters were formed by grouping neighboring crystals having energies above threshold. The highest-energy crystal in a cluster was required to be at least 10 MeV. The position of the shower was then calculated as the energy-weighted mean of all member-crystal positions. Plus, the summed energy deposited in the nearby 9 crystals (3x3 grid) over then energy deposited in the nearby 25 (5x5 grid) should be greater than a certain value. This value, often refers to $e9oe25$, is almost 1 and is used in CLEO's photon selection criteria.

Photons are not charge particles and produce no signal at drift chamber. Showers associated with charged particles were distinguished from photons using loose track-shower matching criteria (no TrackMatch). Photons must not associated with hot crystals.

In summary, cuts used for photon selection are:

1. not hot;

2. no TrackMatch;

3. E9OE25 OK;

4. $E > 30$ MeV, good Barrel or Endcap.

3.3.4 π^0, K_S^0 and η selection and efficiency

We identify π^0 and η candidates via $\pi^0 \to \gamma\gamma$ and $\eta \to \gamma\gamma$. π^0 and η are built by combining photons found in the calorimeters. These photons are subject to cuts discussed in the previous section, and are then combined to see if they could have come from a π^0 or η.

π^0 efficiency determination was done by searching the missing momentum of hadronic decay $D^0 \to K^+\pi^-\pi^0$ with P_{miss} defined by $P_0 - P_{tag} - P_K - P_\pi$. The channel was chosen for its high statistics and low backgrounds. First, a fully reconstructed DTag was found. Events with π^0 correctly reconstructed lie in the diagonal where $|P_{\pi^0}| = |P_{miss}|$ (see Fig 3.1).

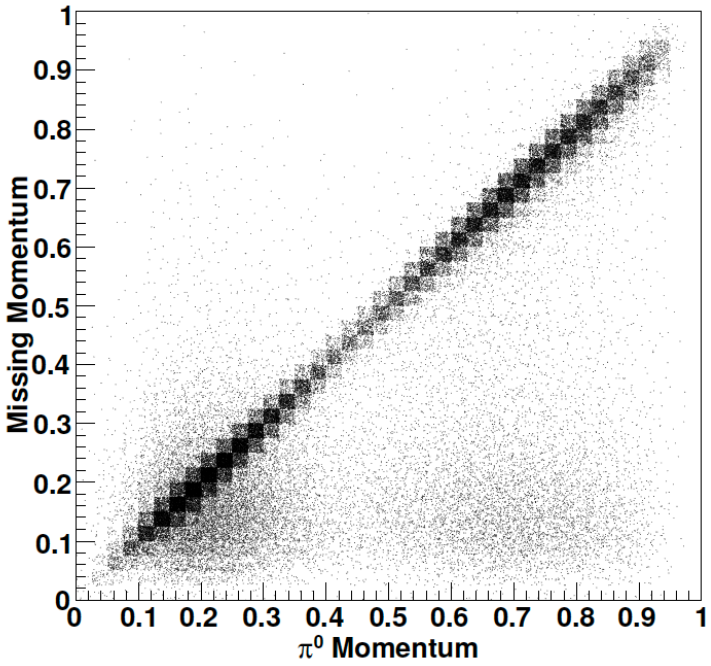

Figure 3.1: $|P_{miss}|$ vs. $|P_{\pi^0}|$ for π^0 efficiency study

The invariant mass of $K\pi\pi^0$ should peak at 1.865GeV. Fig 3.2 shows invariant

mass distribution of $D \to K\pi\pi^0$ when a π^0 was found. Based on the plot, a 60MeV mass cut was applied (red line in figure) to reduce population of fake π^0s in the signal sample. In reference [42], π^0 finding efficiencies was found to be around 50% depending on cuts used. The ratio between data and MC finding efficiencies was about 94% for standard cuts used.

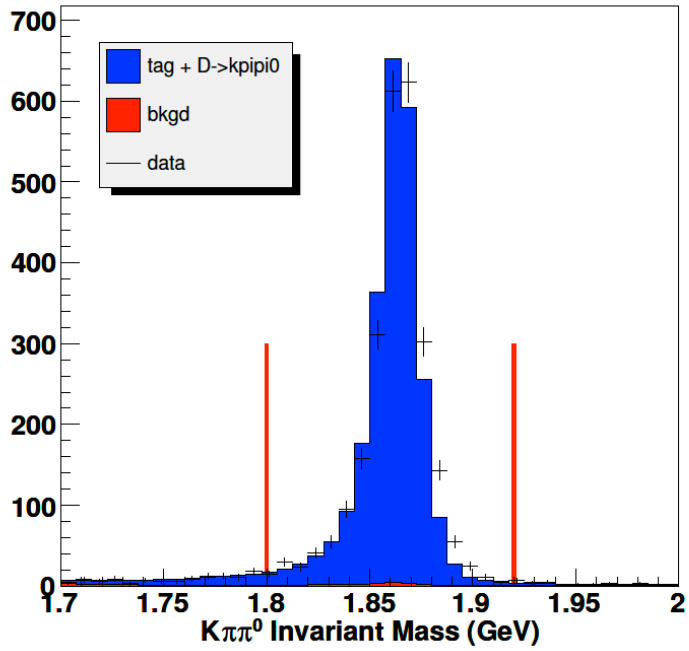

Figure 3.2: Invariant mass of $D \to K\pi\pi^0$ where a π^0 was found. Blue and red dotted show signal and background from signal MC data. Black cross shows Real data.

The K^0_S is built by finding two pion tracks that come together in a shape called a "vee", or vsecondary vertex. Included is the requirement that these charged pions have a total energy that sums to within 30 MeV of the nominal K^0_S mass, 0.4977 MeV. The two pions have no PID requirements, and a vertex fit is done to allow for the K^0_S flight distance. 0.8% systematic uncertainty for each K^0_S is suggested based on the full dataset analysis at CLEO-c[43].

	DTag Selection Requirements
Track quality requirements:	$\chi^2 < 100000$
	$hit/frac > 0.5$
	$\|cot\theta\| < 2.53$
	$\|\bar{p}\|_{Max} > 2.00GeV$
	$\|\bar{p}\|_{Min} > 0.05GeV$
	$\|z_0\| > 0.050m$
	$\|d_b\| > 0.050m$
	standard PID
π^0/η requirements:	$\chi^2 < 10000$
	$\sigma \leq 1000$
	$M_{unconstrained} < 1000GeV$
	$pullMass \leq 3.0$
	$shwrMinE = 30/50MeV$
K_s^0 requirements:	$\chi^2 < 1000$
	$pullMass \leq 3.0$
	$M_{unconstrained} < 1000GeV$

Table 3.2: Selection requirements on DTag object and component particles.

3.4 DTags

The analysis begins with reconstructed D_s mesons called single-tags, or DTags, and that reconstruction is implemented by CLEO-c specific software[44]. DTags are the standard way in CLEO-c of constructing an object representing the decay of a D (D_s) meson from tracks and showers in the detector. The DTag code identifies D_s-meson hadronic decays to many distinct final states, classified by the specific decay products: :$\pi^{\pm}, K^{\pm}, K_s^0, \pi^0$ and η. An event can be fully-reconstructed as a double-tag by joining one DTag with another DTag. The DTag code prevents a track or shower from being used twice in a double-tag; DTags that have any common constituents cannot be joined. A DTag object has already passed a series of standard selection requirements before becoming available; these are listed in Table 3.2 and are explained in greater detail in Reference[44].

The tagged D_s candidate can be either primary or the or the secondary D_s from D_s^*. We require the intermediate states to satisfy mass windows around the nominal

mass (detailed in chapter 4). All charged particles must have momentum above 100 MeV to eliminate the soft pions from $D^*\bar{D}^*$ decays.

A list of CLEO-c D_s tag tables was shown in Fig 3.3. Eight D_s modes are used to measure the D_s production in this analysis. These modes are listed in chapter 4. These tag modes are those with the best signal to background ratio.

400	$D_s^+ \to K_S^0 K^+$
401	$D_s^+ \to K^- K^+ \pi^+$
402	$D_s^+ \to K_S^0 K^+ \pi^0$
403	$D_s^+ \to K_S^0 K_S^0 \pi^+$
404	$D_s^+ \to K^- K^+ \pi^+ \pi^0$
405	$D_s^+ \to K_S^0 K^+ \pi^+ \pi^-$
406	$D_s^+ \to K_S^0 K^- \pi^+ \pi^+$
407	$D_s^+ \to K^- K^+ \pi^+ \pi^+ \pi^-$
420	$D_s^+ \to \pi^+ \pi^0$
421	$D_s^+ \to \pi^+ \pi^+ \pi^-$
422	$D_s^+ \to \pi^+ \pi^+ \pi^- \pi^0$
423	$D_s^+ \to \pi^+ \pi^+ \pi^+ \pi^- \pi^-$
424	$D_s^+ \to \pi^+ \pi^+ \pi^+ \pi^- \pi^- \pi^0$
440	$D_s^+ \to \pi^+ \eta \ (\eta \to \gamma\gamma)$
441	$D_s^+ \to \pi^+ \pi^0 \eta \ (\eta \to \gamma\gamma)$
442	$D_s^+ \to \pi^+ \pi^+ \pi^- \eta \ (\eta \to \gamma\gamma)$
460	$D_s^+ \to \pi^+ \eta' \ (\eta' \to \pi^+ \pi^- \eta, \ \eta \to \gamma\gamma)$
461	$D_s^+ \to \pi^+ \pi^0 \eta' \ (\eta' \to \pi^+ \pi^- \eta, \ \eta \to \gamma\gamma)$
480	$D_s^+ \to \pi^+ \eta' \ (\eta' \to \rho^0 \gamma)$
481	$D_s^+ \to \pi^+ \pi^0 \eta' \ (\eta' \to \rho^0 \gamma)$
500	$D_s^+ \to K_S^0 \pi^+$
501	$D_s^+ \to K_S^0 \pi^+ \pi^0$
502	$D_s^+ \to K^+ \pi^- \pi^+$
503	$D_s^+ \to K^+ \pi^- \pi^+ \pi^0$
504	$D_s^+ \to K^- K^+ K^+$

Figure 3.3: CLEO-c D_s tag modes with CLEO-c mode number showing on the left.

We use the reconstructed invariant mass of the tag (M_{Ds}) and the mass recoiling against the candidate, $M_{recoil} = \sqrt{(E_0 - E_{Ds})^2 - (\vec{p_0} - \vec{p_{Ds}})^2}$ as our primary kinematic variables to select the D_s tag. Here $(E_0, \vec{p_0})$ is the net four-momentum of the beams, taking the finite beam crossing angle into account. Typical mass distributions

are shown in Fig 3.4.

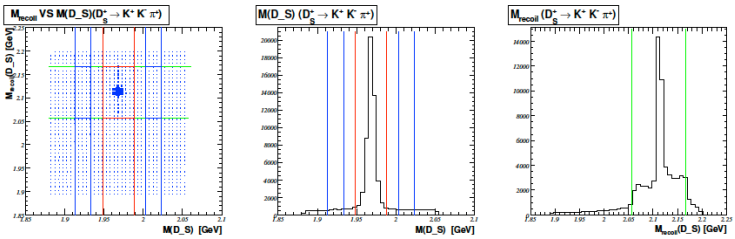

Figure 3.4: M_{recoil} vs. M_{Ds} distribution of channel $D_s \to KK\pi$ from signal MC sample. Red and Green lines reflect signal cuts, blue line shows sideband region

There are two components in the recoil mass distribution: a peak around the D_s^* mass if the tag is due to the primary D_s, and a broad distribution if the tag is due to the secondary D_s from D_s^* decays. The edges of M_{recoil} of the secondary D_s tag are kinematically determined. For tag from primary D_s $\Delta M = M_{recoil} - M_{Ds^*}$=[8.5, 29.8] MeV. For secondary D_s tag, ΔM=[-54.4, 57.1] MeV. We select tags within the range [-55, 55] MeV and look at M_{Ds} distribution to get the number of tags for further analysis. This loose window allows both primary and secondary D_s tags to be selected.

We also require a photon consistent with coming from $D_s^* \to D_s\gamma$ decay, by looking at mass recoiling against tag plus γ system. Here we define $MM^{*2} = \sqrt{(E_0 - E_{Ds} - E_\gamma)^2 - (\vec{p_0} - \vec{p_{Ds}} - \vec{p_\gamma})^2}$. For correct combinations, this recoil mass peaks at M_{Ds} , regardless of whether the candidate is due to a primary or a secondary D_s. We did MC analysis and applied mode dependent cut on MM^{*2}. Except channel $D_s \to \eta\rho$, where we use 2σ cut, we always use 2.5σ cut on other channels. A plot of MM^{*2} distribution in shown in Fig 3.5.

3.4.1 Slow Track Veto and K_S^0 Flight Significance Cut

The bump structures in the tag sideband region of M(D_s) are mainly caused by $D^{*+}D^{*-}$ events followed by $D^{*-} \to \pi^- D^0$ or $D^{*-} \to \pi^0 D^-$ decays. There's also some small contribution from $D^{*0}\bar{D}^{*0}$. Those events are rejected by applying slow pion

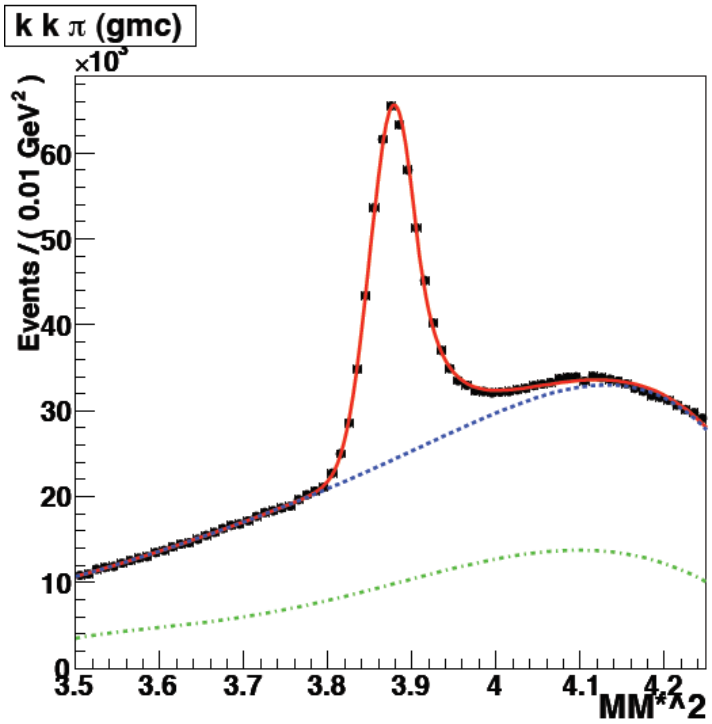

Figure 3.5: MM^{*2} of $D_s \to KK\pi$ from generic MC sample. Blue dotted line shows total background. Green dash-dotted line shows background from fake D_s tags.

veto, reject the D_s candidates with pion momentum below 100 MeV. Kinematically allowed region of slow pions from D^{*-} decays are beam energy dependent and they are below 80.7 MeV for charged pion at 4170MeV. Unfortunately backgrounds from D^* cannot all be removed by slow track veto alone for decay $D_s^- \to K_s^0 K^-$. Further, we require that the K_s^0 has traveled a measurable distance from the interaction point before decaying. For example, the distance along the flight path, from interaction point to K_s^0 decay vertex, be greater than zero with a 3σ significance to remove the bump structure in high sideband region caused by false K_s^0 candidates. After the low-momentum track veto and K_s^0 flight significance requirement are applied, no bump structures remain as shown in Fig 3.6.

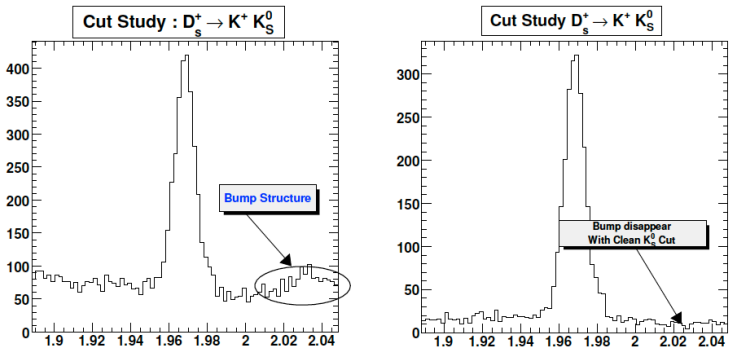

Figure 3.6: $D_s \to KK\pi$ mass distribution before and after π^0 veto and K_s^0 flight significance cut. Data came from signal MC sample.

Chapter 4: Search for the decay $D_s \to \omega e\nu$

4.1 Data analysis method, data samples and Monte Carlo.

The datasets were summarized in Chapter 3. The total integrated luminosity is 586pb^{-1}.

The known charm physics processes are included in the Generic MC (GENMC). All types of charmed mesons production backgrounds, dominant in this analysis, are simulated to 20 times the statistics in the data, while the continuum (u, d, s) backgrounds are simulated to 6.6 times the statistics in the data.

In the following, where MC results are presented, we multiply the small continuum MC sample by 3 to obtain a consistent $\times 20$ normalization. By convention, GENMC refers to the charm part of the MC, continuum MC is the non-charm part, and MC is the weighted sum of the two.

Signal MC events were generated, 10^5 events for each of the 8 tagging modes considered. The same number of events, for each tag mode, was also generated for the $D_s \to \eta e\nu$ and $D_s \to \phi e\nu$ processes.

The analysis starts by looking for an exclusively reconstructed hadronic D_s candidate, the tag, and a single photon candidate. Cuts are imposed on the reconstructed tag mass M_{tag}, the recoil mass M_{rec} and the missing mass squared,

$$MM^{*2} = (E_0 - E_{tag} - E_\gamma)^2 - (\vec{p}_0 - \vec{p}_{tag} - \vec{p}_\gamma)^2. \tag{4.1}$$

$(E_0, \vec{p}_0)$ are the four-momentum of the colliding beams and were defined in Chapter 3. The tag $(E_{tag}, \vec{p}_{tag})$ and photon $(E_\gamma, \vec{p}_\gamma)$ four-momenta are defined likewise. MM^{*2} should peak at $M(D_s)$ squared, if the event is signal.

The rest of the event is the signal candidate. An electron candidate of charge opposite the tag is required, precisely three good tracks, a good π^0, with total event charge equal to zero, and the missing energy and momentum to be in a relation consistent with the presence of a near massless neutrino. Extra photons in the event are ignored.

4.2 Tag selection.

4.2.1 Tag-side cuts.

Eight modes are used, out of nine which have been used for similar analyses.

The tag mass combination is constructed and cuts are applied on the tag mass. The number of events in the mass peak is ultimately determined by a fitting procedure, but it is useful to determine a "peak" region and a "sideband" region (a mass region to either side of the peak) which can be used to study the differences between signal and background.

The tag modes, and their tag mass cuts, are described in Table 4.1. The mass cuts are discussed below.

Table 4.1: Tag modes and signal/sideband cuts

Mode	Number	Signal region (GeV)	Low sideband (GeV)	High sideband (GeV)
$K^0_s K^-$	400	[1.9536, 1.9826]	[1.9100, 1.9390]	[1.9971, 2.0262]
$K^+K^-\pi^-$	401	[1.9539, 1.9822]	[1.9114, 1.9397]	[1.9963, 2.0246]
$K^{\star-}\bar{K^{\star 0}}$	406	[1.9529, 1.9825]	[1.9085, 1.9381]	[1.9973, 2.0269]
$\pi^+\pi^-\pi^-$	421	[1.9546, 1.9824]	[1.9130, 1.9408]	[1.9963, 2.0241]
$\eta\pi^-$	440	[1.9403, 2.0011]	[1.8916, 1.9220]	[2.0193, 2.0497]
$\eta\rho^-$	441	[1.9400, 1.9979]	[1.8850, 1.9139]	[2.0211, 2.0500]
$\pi^-\eta'(\eta\pi^+\pi^-)$	460	[1.9444, 1.9924]	[1.8850, 1.9330]	[2.0040, 2.0520]
$\pi^-\eta'(\rho\gamma)$	480	[1.9440, 1.9920]	[1.8855, 1.9304]	[2.0022, 2.0471]

A cut is also applied to the recoil mass, M_{rec}, defined as

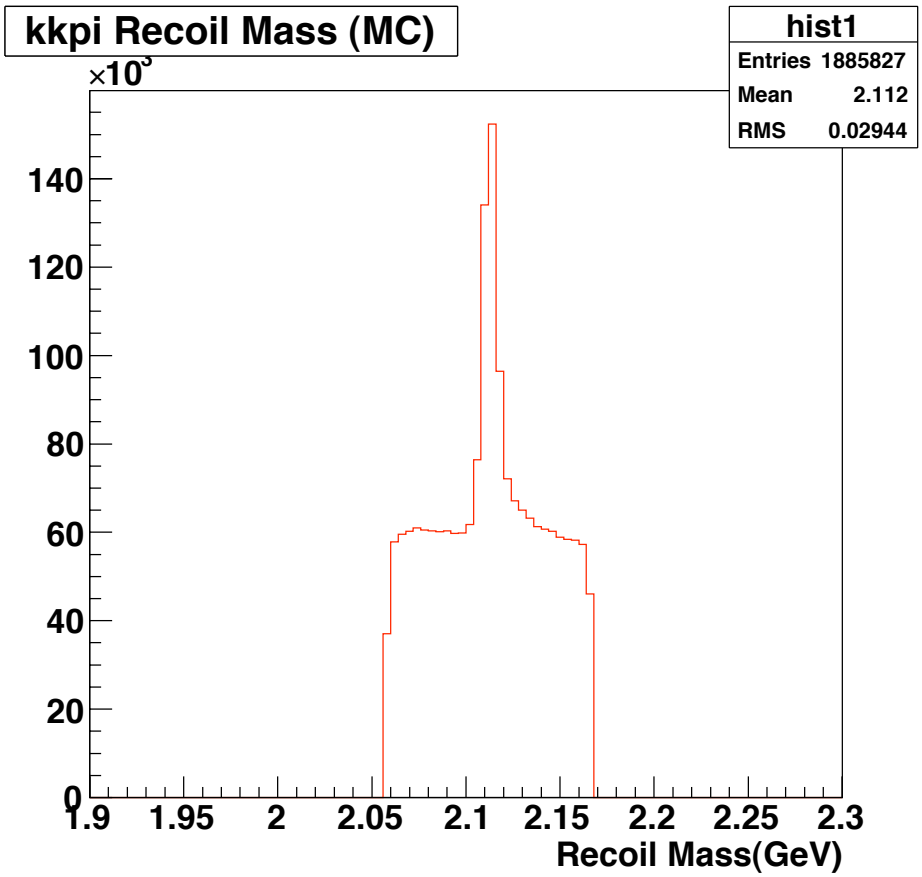

Figure 4.1: Signal MC M_{rec} spectrum. M_{rec} has physical bounds which are used to reduce backgrounds.

$$M_{rec} = \sqrt{(E_0 - E_{tag})^2 - (\vec{p}_0 - \vec{p}_{tag})^2} \tag{4.2}$$

By studying the signal MC spectrum of M_{rec} (Fig. 4.1), it is found that the signal distribution has two components. The sharp peak in the center is the contribution from directly produced D_s, while the broader structure is due to the D_s^* contribution. A ± 55 MeV cut on recoil mass is imposed.

Some mode specific cuts need to be applied. For modes with pions, the momentum of pions is required to be greater than $100 MeV$ so that soft pions coming from $D^{*-} \rightarrow \pi^- D^0$ are removed. For modes with K_s^0, CLEO II style TCleanV0c [45]

and RareB [46] cuts are used, to reduce fake K_s^0. Mass cuts are also used on some of the tag modes. Extra cuts on tag side particles are summarized below. The K_s^0 cuts are discussed in more detail in the next Subsection.

- $D_s^- \to K^- K^+ \pi^-$, $p_\pi > 0.1$ GeV.
- $D_s^- \to K_s^0 K^-$. $(M_{K_s^0} - 0.4977)/0.004 < 3$,

  TCleanV0c: $prob() > 0$, $chisq() > 0$, $fvsgnf() > 3$ and $Cleo2RareBK0s()$.
- $D_s^- \to \pi^- \eta$. $\eta \to \gamma\gamma$ is from the η table.
- $D_s^- \to \eta\prime \pi^-$. $(\eta\prime \to \pi^+\pi^-\eta)$ only. $\eta \to \gamma\gamma$ is from the η table.
- $D_s^- \to \pi^+\pi^-\pi^-$, $p_\pi > 0.1 GeV$.
- $D_s^- \to K^{*-}\bar{K}^{*0}$. Only the $(K_s\pi^-)(K^+\pi^-)$ channel is considered.

  $(M_{K_s^0} - 0.4977)/0.004 < 3$.

  TCleanV0c: $prob() > 0$, $chisq() > 0$, $fvsgnf() > 3$ and $Cleo2RareBK0s()$.

  K^{*-} and $\bar{K}^{*0}$ mass within $100 MeV$ of PDG value.
- $D_s^- \to \eta\rho^-(\rho^- \to \pi^-\pi^0)$. $\eta \to \gamma\gamma$ is from the η table. ρ^- mass within $150 MeV$ of PDG value.
- $D_s^- \to \pi^-\eta\prime(\eta\prime \to \rho\gamma), \rho \to \pi^+\pi^-$

  $\eta\prime$ mass within $20 MeV$ of PDG value.

  π $\eta\prime$ helicity cut: $|cos\theta| < 0.8$.

The M_{tag} distributions for the 8 modes are shown in Figs. 4.2 and 4.3, for MC and data, respectively.

They are fitted with a peak consisting of a double Gaussian, plus a linear background. The function used is listed here, with M_{Ds} being the nominal D_s mass, or

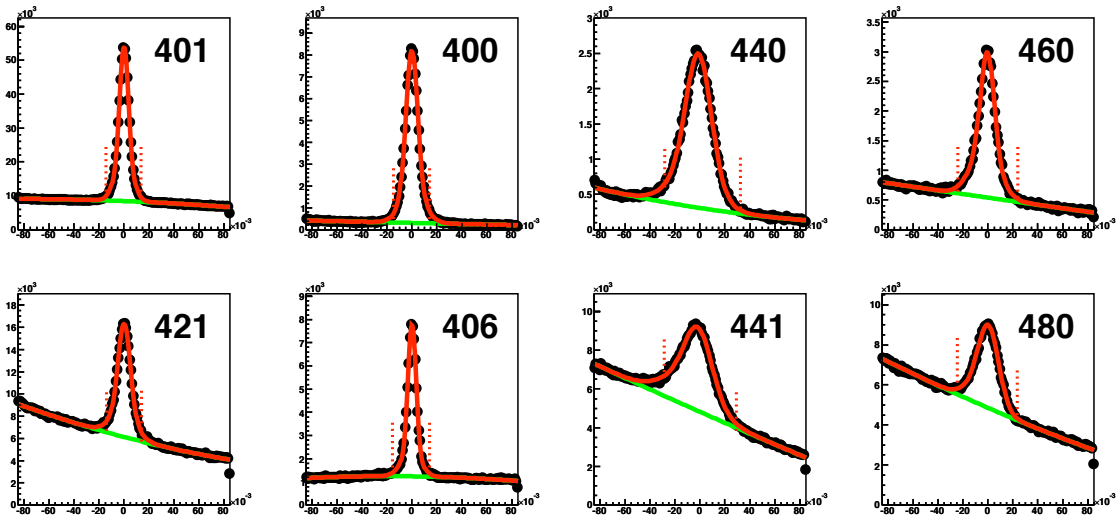

Figure 4.2: Generic MC Invariant mass distribution of D_s candidates. Mode 401 (a): $K^+K^-\pi^-$; Mode 400 (b): $K^0_sK^-$; Mode 440 (c): $\eta\pi^-$; Mode 460 (d): $\pi^-\eta'(\eta\pi^+\pi^-)$; Mode 421 (e): $\pi^+\pi^-\pi^-$; Mode 406 (f): $K^{\star-}\bar{K}^{\star0}$; Mode 441 (g): $\eta\rho^-$; Mode 480 (h): $\pi^-\eta'(\rho\gamma)$. Also shown are the mass cuts for each mode.

1.9685 GeV [14], and $G(x;\sigma,\mu)$ being the Gaussian of area one, width σ and peaking at μ

$$f(M_{tag}) = N(f_1 G(M_{tag};\sigma_1,M_{Ds}) + (1-f_1)G(M_{tag};\sigma_2,M_{Ds})) + \Sigma_{i=0}^{1} a_i M_{tag}^i. \quad (4.3)$$

The free parameter N provides the number of tag events for each mode. The M_{tag} MC and data fit results are listed in Table 4.2. Note that for data fit the peak parameters are assumed to be those obtained in the GENMC fit, while the background parameters are fitted independently. The scale factor in the last column is defined as the integrated background in the signal region (the integral of the fitted function) divided by the integrated background in the sideband region. The rest of the fit parameters are listed in Table 4.3.

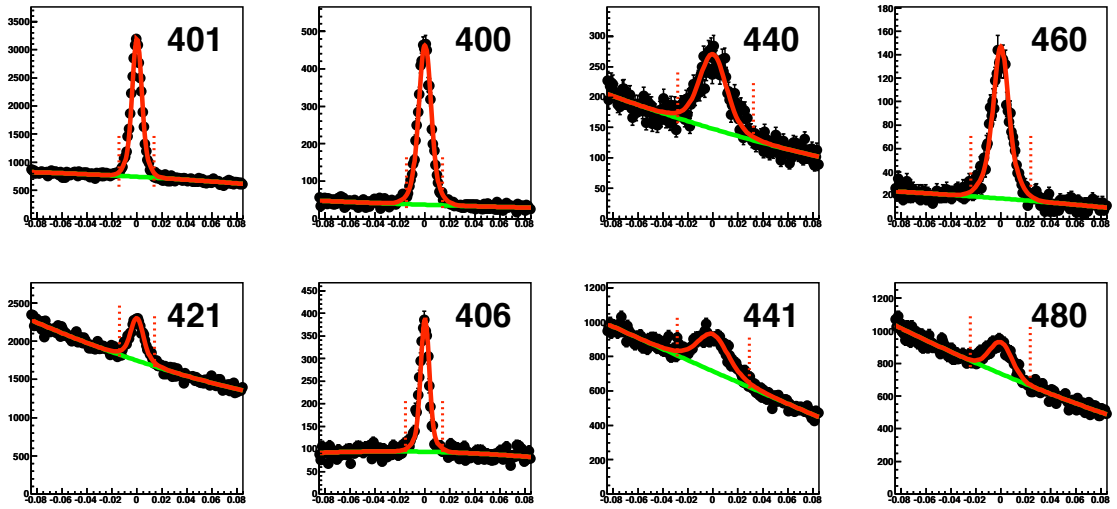

Figure 4.3: Real data invariant mass distribution of D_s candidates. Mode 401: $K^+K^-\pi^-$; Mode 400: $K^0_sK^-$; Mode 440: $\eta\pi^-$; Mode 460: $\pi^-\eta'(\eta\pi^+\pi^-)$; Mode 421: $\pi^+\pi^-\pi^-$; Mode 406: $K^{\star-}\bar{K^{\star0}}$; Mode 441: $\eta\rho^-$; Mode 480: $\pi^-\eta'(\rho\gamma)$. Also shown are the mass cuts for each mode.

The mass cuts in Table 4.1 are chosen at 2.5 R.M.S. from the fitted peak position for each mode except for the $(\eta\rho)$ mode which is cut at 2R.M.S. R.M.S. is defined as $(\text{R.M.S.})^2 = f_1\sigma_1^2 + (1-f_1)\sigma_2^2$.

4.2.2 CleanV0.

The Cleo-c software does not provide fake vertex rejection as good as the CleoII.V software. To improve signal to noise, non-standard cuts are used to select viable K_s candidates using cuts that simulate a software package used in previous editions of CLEO, called CLEANV0. This package was used to reject combinations of tracks which could simulate a detached vertex. With the exception of a different mass cut (12 as opposed to 10 MeV), the cuts described in Section 3.4 are the same as those in CLEANV0.

The CLEANV0 uses momentum dependent cuts. For a vertex momentum $p_V <$ 2.5 GeV, they are listed here:

Table 4.2: Tag D_s mass fitting result

Modes	N_{data}	N_{GENMC}	Low Sideband	High Sideband	Scale Factor
$K_s^0K^-$	5828.4 ± 92.3	98809	1231.4	958.2	0.4954 ± 0.0129
$K^+K^-\pi^-$	25989.6 ± 284.8	457923	22385.1	19451.6	0.5037 ± 0.0027
$K^{\star-}\bar{K^{\star 0}}$	2891.1 ± 100.4	44366	2783.4	2646.8	0.5106 ± 0.0076
$\pi^+\pi^-\pi^-$	8152.1 ± 368.5	134496	56530.3	43475.2	0.4950 ± 0.0018
$\eta\pi^-$	3634.6 ± 159.6	58618	5727.9	3378.8	0.9797 ± 0.0071
$\eta\rho^-$	6877.1 ± 329.5	129827	26879.3	14658.4	0.9958 ± 0.0033
$\pi^-\eta'(\eta\pi^+\pi^-)$	2344.2 ± 69.7	41420	1039.5	571.8	0.5123 ± 0.0192
$\pi^-\eta'(\rho\gamma)$	4451.3 ± 337.3	86898	42411.6	25475.6	0.5226 ± 0.0029

Table 4.3: Tag mass fit results.

Tag mass fit results. The peak parameters are obtained from the GENMC fits, and used to fit the data also. The linear background parameters are fitted independently in the MC and data and labeled accordingly.

Mode	f_1	σ_1 (MeV)	σ_2 (MeV)	a_0 (MC)	a_1 (MC)	a_0 (D)	a_1 (D)
$K_s^0K^-$	0.471	4.05	7.00	-1.73	-5.42	-2.93	4.09
$K^+K^-\pi^-$	0.725	3.74	8.92	-3.68	-19.33	-1.64	-4.20
$K^{*-}\bar{K^{*0}}$	0.771	3.430	10.65	-5.81	-11.23	-0.571	-10.50
$\pi^+\pi^-\pi^-$	0.899	4.84	9.88	-4.81	11.03	-3.11	5.58
$\eta\pi^-$	0.650	9.85	15.56	-8.46	15.38	-4.12	5.30
$\eta\rho^-$	0.574	10.8	18.3	-5.89	-0.752	-0.581	-11.24
$\pi^-\eta'(\eta\pi^+\pi^-)$	0.590	5.71	13.34	-5.93	7.03	-4.76	-6.66
$\pi^-\eta'(\rho\gamma)$	-	9.60	-	-5.54	3.97	-4.37	4.54

- two tracks, no z-escape or dredge daughter tracks (minimal quality cuts to reject loopers);
- track fit to common vertex successful ($CHIVTX > 0$ and $P(\chi^2) > 0$).
- vertex distance to the IP $FVSGNF > x$ standard deviations along the flight direction. $x = 3$ if $p_V \leq 1$ GeV, $x = 5.5$ if $p_V > 1$ GeV.
- both tracks have a large χ^2 when fitted to the IP ($CHVDAU_i > 2.5$).
- each track must have a transverse impact parameter less than 3.5 standard

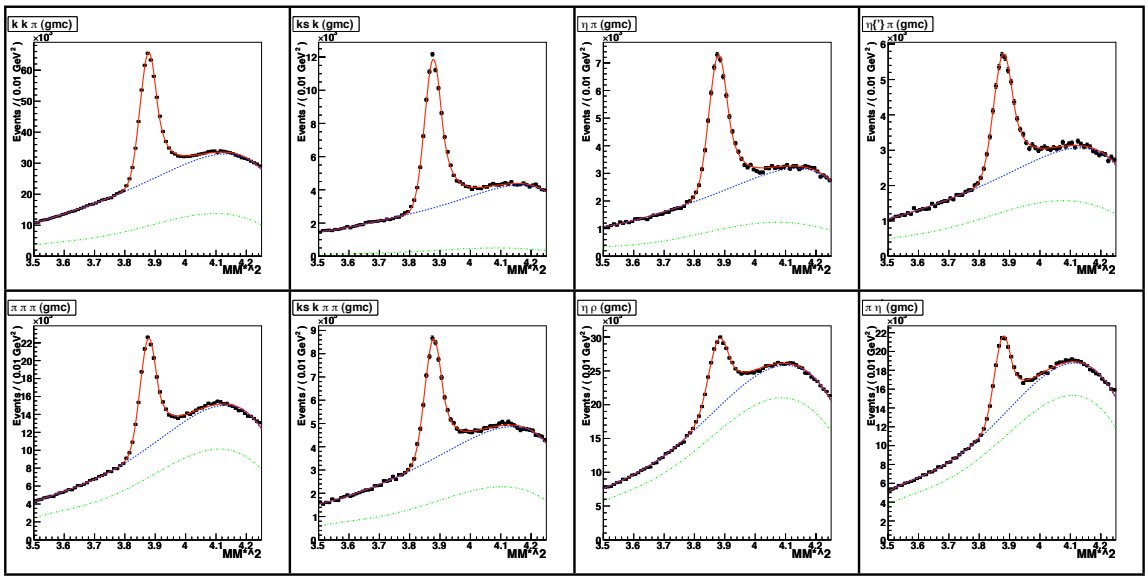

Figure 4.4: GENMC MM^{*2} distributions for the 8 tag modes. Green dash-dotted ones are the BG2 background defined in the text. Blue dashed ones are the total background.

deviations ($RMSTX_i/DRMSTX_i < 3.5$).

- the pion-pion mass, $M_{\pi\pi}$, must be within 10 MeV of the nominal K_s mass. This corresponds to roughly a 3σ mass cut.

In practice, the last cut is the most important one. Although some analyses do not depend on K_s purity, some still do, and this is one of them. Two examples:

- Ref. [42] applies only the $M_{\pi\pi}$ cut to clean its K_s sample;
- Our own analysis, $D^+ \to \phi l\nu$ (same process as the one sought in this analysis), presented by Peng Zhou at the Cleo 2009 July meeting, finds that GENMC backgrounds are dominated by fake tags which include a fake K_s (11 out of 12 surviving events). The $M_{\pi\pi}$ cut alone eliminated all 11 events.

To summarize the effects of a CLEANV0 cut on the present analysis, Table 4.5 is shown (compare also with Table 4.2). For the two tag modes containing a K_s^0, the signal increases by 12% and 31%, when the CLEANV0 cut is removed. The

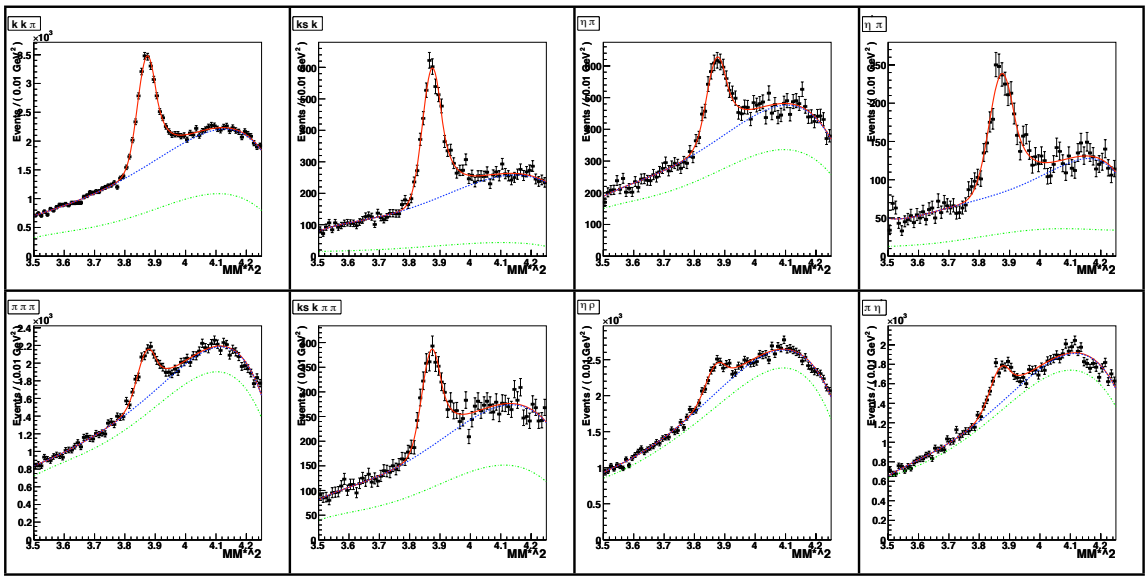

Figure 4.5: Data MM^{*2} distributions for the 8 tag modes. Green dash-dotted ones are BG2. Blue dashed ones are total background.

backgrounds, however, increase by factors of 3 and 3.5 respectively. The 2-D fits (M_{tag}, MM^{*2}) for the data were also redone without CLEANV0 to show that the total signal reduction rate is similar to the M_{tag} 1-D fit (13% and 35% respectively).

With analysis being dominated by background fluctuations, the CLEANV0 cut is helpful.

4.2.3 MM^{*2}.

The MM^{*2} mass cuts are found by a 2-D binned likelihood fitting the distribution in the (MM^{*2}, M_{tag}) space. Each projection is also kinematically fitted, so that M_{tag} is the value obtained by constraining MM^{*2} to its nominal value, and viceversa. This procedure also minimizes any correlation between the two variables.

In this 2D fit:

- The Signal PDF is the product of a double gaussian (the M_{tag} projection) and a Crystal Ball shape (the MM^{*2} projection).

Table 4.4: MM^{*2} cuts and N_{tag} fit results.

Modes	Lower cut (GeV^2)	Upper cut (GeV^2)	N_i(data)	N_i(GENMC)
$K_s^0K^-$	3.78759	3.95394	3442 ± 138	65804 ± 830
$K^+K^-\pi^-$	3.79394	3.95096	15647 ± 271	304958 ± 1314
$K^{\star-}\bar{K^{\star 0}}$	3.75048	3.98465	1707 ± 94	40452 ± 515
$\pi^+\pi^-\pi^-$	3.77005	3.96327	4595 ± 298	89260 ± 783
$\eta\pi^-$	3.76617	3.97979	2355 ± 187	41783 ± 651
$\eta\rho^-$	3.76983	3.96322	3606 ± 640	89093 ± 1036
$\pi^-\eta'(\eta\pi^+\pi^-)$	3.74087	3.98878	1716 ± 142	30185 ± 614
$\pi^-\eta'(\rho\gamma)$	3.78752	3.96008	3373 ± 240	62301 ± 810
N_{tag}	-	-	36441 ± 852	723836 ± 2413

- One of the background component is the combination of a real tag with a random γ. This type of background (BG1) is described by the same double gaussian shape (M_{tag}) and a 5th order polynomial (MM^{*2}).

- The other background (BG2: Green dash-dotted ones in plots) is due to fake tags. PDF here is the product of a 1st order polynomial (M_{tag}) and a 5th order polynomial (MM^{*2}).

- Finally, the data are fitted with the signal function obtained in the GENMC fit, but the background parameters are varied

The 1D projections of MM^{*2} are shown in Fig. 4.4 and Fig. 4.5. Based on the fitting parameters, the cuts on MM^{*2} are summarised in Table 4.4.

Table 4.4 also lists the final number of tags obtained in each tag mode, N_i, as well as the total number of tags, N_{tag}, used to extract the final result.

4.2.4 Signal cuts.

The signal is selected by requiring one electron candidate, of charge opposite to the tag, two charged pion candidates, of opposite charge, no extra good tracks, and

Table 4.5: Effect of CLEANV0 cut on tag and tag background rates.

Mode	Signal	Low sideband	High sideband	(M_{tag}, MM^{*2})
$K_s^0 K^-$				
CleanV0 (Data)	5828 ± 92	1231	958	3442 ± 138
No CleanV0 (Data)	6524 ± 121	3317	3175	3896 ± 160
CleanV0 (Signal MC)	16995 ± 131	71	48	N/A
No CleanV0 (Signal MC)	19004 ± 140	168	110	N/A
$K^{\star -} K^{\star 0}$				
CleanV0 (Data)	2891 ± 100	2783	2647	1707 ± 93
No CleanV0 (Data)	3782 ± 181	9842	8999	2310 ± 181
CleanV0 (Signal MC)	9177 ± 103	547	430	N/A
No CleanV0 (Signal MC)	12557 ± 125	1142	914	N/A

a good π^0, all selected exclusively of the objects used in the tag. In case of multiple candidates, the selected π^0 is the one with the best pull mass.

Together they form the 4-vector $(E_s, \vec{p}_s)$. The measured neutrino candidate mass squared, MM^2, is defined as

$$MM^2 = (E_0 - E_{tag} - E_\gamma - E_s)^2 - (\vec{p}_0 - \vec{p}_{tag} - \vec{p}_\gamma - \vec{p}_s)^2,$$

.

The MM^2 distributions of the two control samples $\eta e\nu$ and $\phi e\nu$ are shown in Fig. 4.6, both for data and GENMC. Based on the shape of MM^2, events with $-0.05 < MM^2 < 0.05$ GeV^2 are selected for the final analysis.

In summary, signal cuts consist of

- one electron, $Q_e + Q_{tag} = 0$
- two good charged π, $Q_1 + Q_2 = 0$
- one good, best candidate π^0
- $-0.05 < MM^2 < 0.05$ GeV^2.

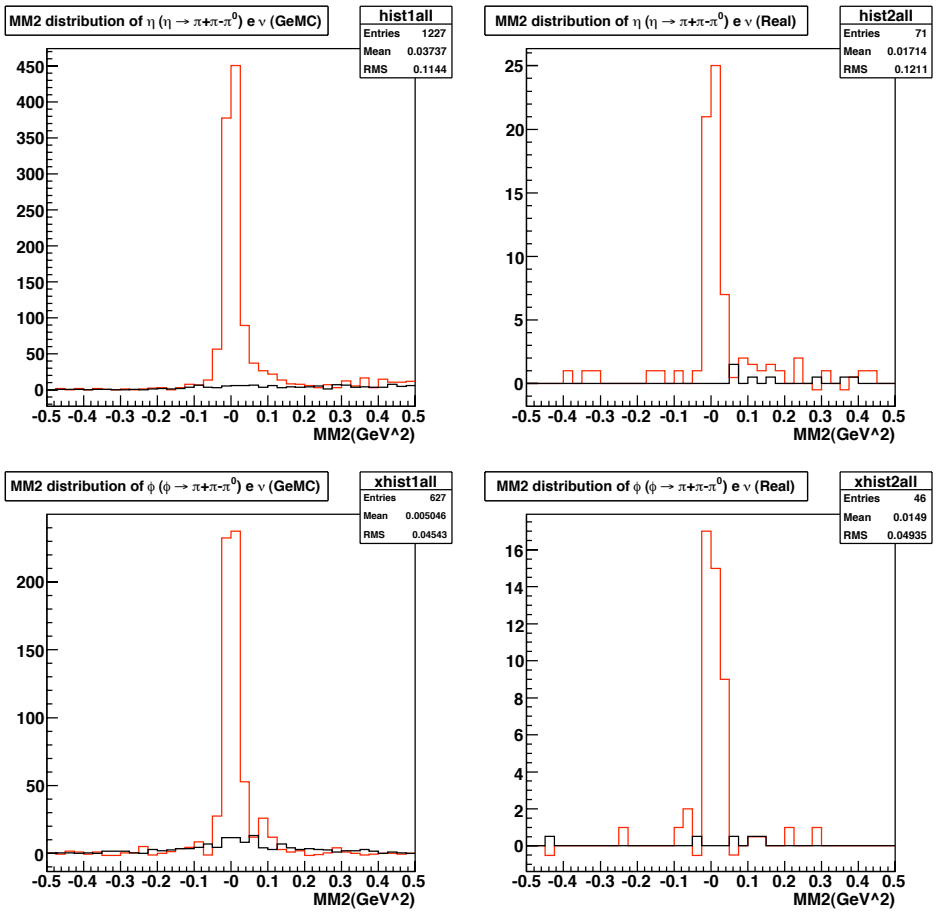

Figure 4.6: MM^2 distributions. Top row: $D_s \to \eta e\nu$. Bottom row: $D_s \to \phi e\nu$. Red histograms: data. Black histograms: GENMC. Left column: Generic MC. Right column: Real data.

4.2.5 Mode selection.

25 D_s decay modes are available in the D_s skims, of which 9 have been selected in the past for their good signal to noise ratio. After having established the analysis cuts, we decided to analyze the fractions of signal and background for each tag mode. A study of the distribution of background and signal by tag mode revealed a further available cut to improve the statistical power of the analysis.

In Table 4.6 the tag mode, the number of real tags in the data, and the number of MC background tags N_B, in the mass region of interest (which is ± 125 MeV from the ω peak and is discussed below) are listed. For completeness, the mode distribution

of the MC tags, N_S, is also shown, but not used.

We construct the relative fraction for each mode and the number of background events, for data and MC

$$\epsilon_d = \frac{N_i}{\Sigma N_i}, \quad \epsilon_B = \frac{N_B}{\Sigma N_B}.$$

We then construct the figure of merit

$$(S/\sqrt{B}) = \frac{1-\epsilon_d}{\sqrt{1-\epsilon_B}}.$$

These quantities are listed in Table 4.6. A figure of merit below 1 implies that the overall statistical error worsens, if the mode is subtracted. A figure of merit above 1 means that the overall statistical error improves, if the mode is subtracted. Clearly only the mode $K^-K^+\pi^-\pi^0$ should be eliminated and we do the final analysis on the other eight modes only.

Table 4.6: Signal to background tag mode fractions for each mode.
Signal to background tag mode fractions for each mode. All quantities defined in the text.

Mode	N_d	N_S	N_B	ϵ_S	ϵ_B	$S/\sqrt{B}$
$K^0_sK^-$	3442.	65804	9.	0.0824	0.0226	0.928
$K^+K^-\pi^-$	15647.	304958.	144.	0.375	0.362	0.782
$K^+K^-\pi^-\pi^0$	5330.	97895.	134.	0.1276	0.337	1.071
$K^{\star-}\bar{K^{\star 0}}$	2025.	40452.	27.	0.0485	0.0678	0.985
$\pi^+\pi^-\pi^-$	4595.	89260.	26.	0.110	0.0653	0.920
$\eta\pi^-$	2355.	41783.	4.	0.0564	0.0100	0.939
$\eta\rho^-$	4425.	89093.	24.	0.106	0.0603	0.922
$\pi^-\eta'(\eta\pi^+\pi^-)$	1716.	30185.	8.	0.0411	0.0201	0.969
$\pi^-\eta'(\rho\gamma)$	3373.	62301.	22.	0.0807	0.0553	0.946
Total	41771	723836	398	-	-	-

4.2.6 M_3 distribution.

Given the analysis discussed in the preceding part of this Section, a M_3 spectrum is obtained. M_3 was not used in our selection, and provides the spectrum that is fitted to extract the final result. In Fig. 4.7 the M_3 spectrum is presented for data and Monte Carlo, including M_{tag} sideband contributions.

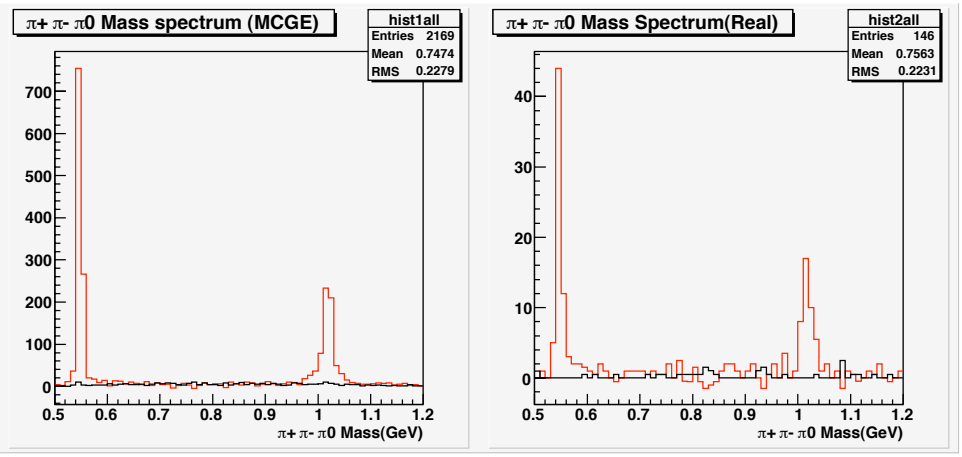

Figure 4.7: $\pi^+\pi^-\pi^0$ (M_3) Mass distribution. Red: M_{tag}, MM^{*2} signal region. Black: M_{tag} sideband contribution. Left: Generic MC. Right: data.

Two peaks are clearly present, at the η and ϕ masses, with no sign of a signal in the ω mass region.

4.3 Signal Monte Carlo and determination of signal efficiency.

The signal MC sample consists of 8×10^5 $D_s \to \omega l\nu$ events generated according to phase space distribution. Equivalent samples were generated for the $\eta e\nu$ and $\phi e\nu$ decays.

The M_3 peaks in MC and signal MC are fitted to a double Gaussian, convoluted with a Breit Wigner shape in the case of ω and ϕ,

$$s(x) = K \int BW(x_1)(f_1 G(x_1;\sigma_1,x) + (1-f_1)G(x_1;\sigma_2,x))dx_1, \qquad (4.4)$$

where K is a normalization constant. Table 4.7 lists the fit results for each of the signal MC generated for this analysis.

Table 4.7: Fitting result for all three channels.

Decay	f_1	σ_1 (MeV)	σ_2 (MeV)	R.M.S. (MeV)
$\eta e\nu$	0.8844	3.165	19.85	7.37
$\omega e\nu$	0.8783	5.500	22.52	9.40
$\phi e\nu$	0.8361	5.940	19.83	9.73

The reconstruction efficiency ϵ is computed by applying the same cuts to the signal MC events, but correcting for the number of tags found in the data

$$\epsilon = \frac{1}{N_{tag}} \Sigma N_i \epsilon_i \tag{4.5}$$

ϵ_i is the signal MC efficiency for mode i. The result is $\epsilon = (5.52 \pm 0.15)\%$.

Finally, both the GENMC and the signal MC were used to estimate the individual contribution of each tag mode to both signal and background. This information, in turn, was used to choose which modes should be used in the final analysis.

4.4 Final fit.

Fig. 4.8 shows the same M_3 plots shown in Fig. 4.7, but they are shown separately and only for the 250 MeV mass region centered at the ω nominal mass. The comparison between data and MC is shown in Fig. 4.9.

In considering the form of final fit, the following is taken into account:

- the statistics in the ω region is low. A broad fit interval, $\Delta_{M3} = 250$ MeV, centered at the nominal ω mass, is used, to minimize the background subtraction error. In this interval, there are $N_{ev} = 18$ events in the data, $N_{ev} = 240$ in the GENMC and $N_{ev} = 8$ events in the continuum MC.

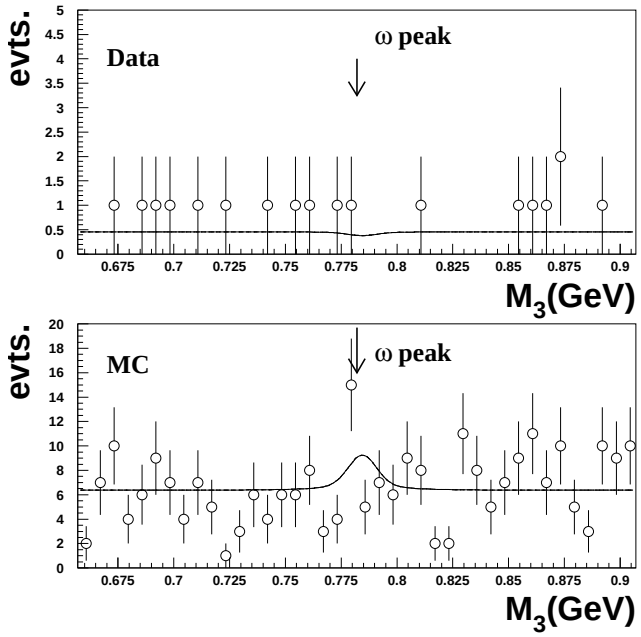

Figure 4.8: $\pi^+\pi^-\pi^0$ (M_3) Mass distribution in the 250 MeV wide region centered at the ω nominal mass. The continuous lines are the fit results, as described in the text. Top: Final data. Bottom: Monte Carlo.

- M_{tag} sideband subtraction would increase the statistical error considerably. There are 15 events in the sideband M_3 spectrum, (Fig. 4.7), which corresponds to a 35% statistical error increase assuming zero signal. Further, M_{tag} sideband subtraction can not be considered a complete background subtraction procedure, since, as we will see below, the irreducible background are in fact dominated by D_s backgrounds.

Three potential sources of background are considered: non-D_s backgrounds, D_s backgrounds where there are non-resonant final states, and D_s backgrounds where

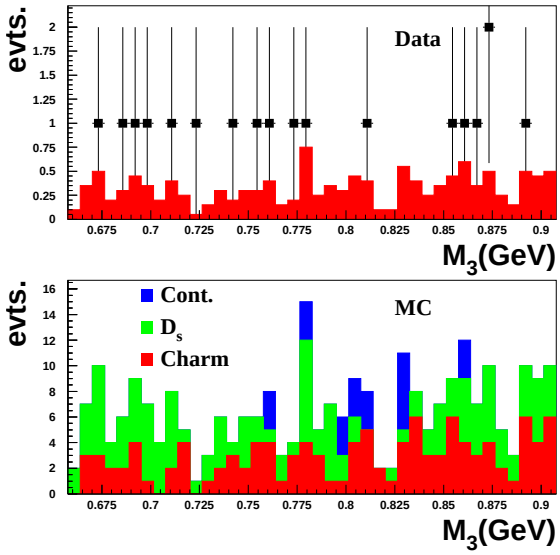

Figure 4.9: Monte Carlo $\pi^+\pi^-\pi^0$ (M_3) Mass distribution in the 250 MeV wide region centered at the ω nominal mass. Top: comparison of final data sample and total Monte Carlo background. Bottom: Total MC, normalized to 20 times the data statistics. Red: charm non D_s backgrounds. Green: D_s backgrounds. Blue: non-charm backgrounds.

there is a true ω. M_{tag} sideband subtraction only subtracts the first source. A direct fit of a signal and a background component subtracts the first two. The third source of background is subtracted via Monte Carlo, and is discussed below.

Our final choice of fitting procedure is a one parameter unbinned likelihood [14]. The free parameter is the total number of signal events S. The background level is constrained by the normalization of the probability.

S is multiplied by a function of unit area $s(x)$, Eq. 4.4. The final expression of

the unbinned likelihood is

$$P(M_{3i}) = P_i = (S/N_{ev})s(M_{3i}) + (1 - S/N_{ev})/\Delta_{M3}, \quad L = \Pi_i P_i, \tag{4.6}$$

which corresponds to a signal unit function, obtained by convoluting the ω Breit-Wigner with the experimental resolution, plus a flat background.

Fig. 4.10 shows the likelihoods obtained for data and MC respectively, in the $S > 0$ region. The 95% C.L. is calculated using only the $S > 0$ portion of the likelihood. A statistical only, 95% CL upper limit for S, $S_{95} = 4.63$ events, is obtained.

Unbinned likelihood fits, in one dimension, can be tested for goodness of fit. The most restrictive test is the Cramer-Von Mises test[47], where the goodness of fit parameter is

$$G = \int_{min}^{max} (F - F_N)^2 dF(M_3). \tag{4.7}$$

Here, the integral limits are the limits of the fit interval. F is the integrated probability function for best parameters, $F = \int_{min}^{M3} P_{max} d(M_3')$. The physical signal with maximal likelihood here is $S = 0$, so that F is a straight line and $dF(M_3) = dx$, with $x = (M_3 - min)/\Delta_{M3}$.

F_N is the step function such that $F_N(M_3) = N/N_{ev}$, where N is the rank of the largest event mass which is less than M_3. The two functions are shown on the left side of Fig. 4.11.

To compare the obtained value of G against a population of unbiased fits, a toy Monte Carlo was run, with 10^4 unbiased experiments being generated. The obtained distribution of G was compared against the value obtained in the final fit. The result is that only 13.16% of the generated experiments was better than the value obtained in the final fit, on the right side of Fig. 4.11.

The toy MC also made it easy to apply the Kolmogorov-Smirnoff test, which

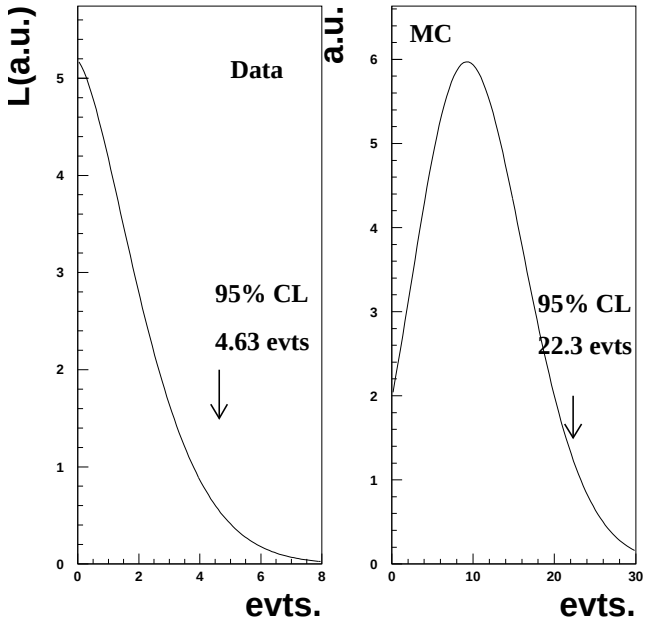

Figure 4.10: Results of a fit to the plots from Fig. 4.8 using the likelihood from Eq. 4.6. The 95% CL was computed using only the positive signal region. Left: Shape of Data likelihood vs. fitted signal. Right: Shape of MC likelihood vs. fitted signal.

simply computes the area between the two curves. In this case, the toy MC could produce a better G only in 15.94% of the unbiased experiments. We conclude that the fit to the data is excellent.

The unbinned fit result to the MC M_3 distribution can also be expressed as (9.2 ± 9.5) events. For comparison purposes, and to produce a significant χ^2, we also fitted the MC distribution with a binned likelihood (40 bins), assuming Poissonian statistics and two parameters (signal and background). For the binned likelihood, we obtained (8.1 ± 8.5) events with a χ^2 of 54.8/38.

Table 4.8: Summary of statistical and systematic errors of S_{95}. Irr. bkg. I and II are described in the text.

Type	Cent. val. (evts.)	σ (evts.)	Comment
Data fit	-0.25	2.21	Main data fit
MC fit	9.2	9.5	MC fit
ω mass	-	0.03	Final fit
ω width	-	0.006	Final fit
Irr. Bkg. I	-0.53	0.19	$D_s \to \eta\prime e\nu$
Irr. Bkg. II	-0.02	0.05	$D_s \to \omega X$
Irr. Bkg. III	-0.15	0.15	Continuum

4.5 Determination of branching ratio and systematic errors.

The statistical upper limit on the number of events is translated into a statistical only limit on the branching ratio according to the following equation

$$B_{95} = \frac{S_{95}}{\epsilon N_{tag}}. \tag{4.8}$$

There are three quantities on the right hand side of Eq. 4.8, with central values yielding $B_{95} = 0.231\%$. Each of the three quantities has a statistical and systematic error which are discussed below.

4.5.1 S_{95} errors.

Table 4.8, first row, contains the relevant parameters of the unbinned likelihood (Fig. 4.8), in the form $\mu \pm \sigma$. μ is the S value for which L_u is maximal, allowing also $S < 0$ values.

For completeness, the GENMC likelihood values are also listed in Table 4.8 . The observed likelihood peaks for both data and GENMC are not uncommon, if the true value of S is zero.

Systematic errors to S_{95} are also listed in Table 4.8 and include:

- ω mass uncertainty. A ± 0.12 MeV shift[14] will change the fit result by ± 0.03

events.

- ω width uncertainty. A ± 0.08 MeV shift[14] will change the fit result by ± 0.006 events.

The greatest source of S_{95} systematic errors, however, are irreducible backgrounds. The GENMC has a small signal of (3.4 ± 9.2) events.

Fig. 4.9 shows the background distribution by physical source. All but one of the true ω within 8 MeV of the ω mass are due to the decay chain $D_s \to \eta\prime e\nu$ (B.R.$= 1.12 \pm 0.35\%$), followed by $\eta\prime \to \omega\gamma$, (B.R.$= 3.02 \pm 0.33\%$)[14].

A dedicated MC for this channel generated 5000 such events (96 times the data), using the $KK\pi$ tag alone, and resulting in 1340 tagged events. This source of backgrounds is listed as Irr. Bkg. I in Table 4.8.

Of the 5000 events, 51 passed all cuts. The expected number of events in the GENMC due to this channel is equal to $(10.6 \pm 1.5 \pm 3.5)$ events. The first error is due to MC statistics and the second is due to the (systematic) branching ratio uncertainties.

This corresponds to an irreducible background of (0.53 ± 0.19) events. Note that the largest source of error is the semileptonic B.R. error from the Particle Data Book. This source of systematics can not be significantly improved with further simulation.

Second, a small signal in the GENMC could be expected, due to irreducible backgrounds from $D_s\omega X$ events. This source of backgrounds is listed as Irr. Bkg. II in Table 4.8. By perusing the QQID information of the GENMC, zero events are found from the direct decay $D_s \to \omega\pi$.

The GENMC significantly underestimates the $(D_s\omega X)$ yield, which is 0.6% in the GENMC but 6.1% in data [48]. The decay $D_s \to \omega\pi^+$ is in the GENMC, but no other $\omega n(\pi)$ decays. Ref. [48] quotes the exclusive branching ratio $D_s \to \omega\pi^+\pi^0$ to be $(2.78 \pm 0.69)\%$, which accounts for about half the $(D_s\omega n(\pi))$ branching ratio.

To address this source of systematic error, we generated and reconstructed 200,000 $D_s \to \omega\pi^+\pi^0$ events ($KK\pi$ tag alone), resulting in about 53500 tags. It is assumed that these will estimate the background from all missing $\omega n(\pi), n > 1$ events. In such case, the generated statistics corresponds to about 23.5 times the number of such expected decays in the data. There were zero signal candidates. We quote this error as 0.02 ± 0.05 events.

Third, there was one more true ω event, within 8 MeV of the peak, which is in the continuum MC, corresponding to one more irreducible background III of 0.15 ± 0.15 events. The total, recalculated number of events in the MC peak is $0.7times20$, or 14 events, in good agreement with the fitted value of (9.2 ± 9.5).

4.5.2 N_{tag} errors.

Because N_{tag} is obtained through a fit, systematic errors can enter the analysis only through the bias in the choice of fitting function. This can be quantified by varying the fitting function in a variety of ways.

For each tag mode, the fitting function was changed as follows:

- Change in signal modeling. The Crystal Ball function was varied in two ways, by keeping the n parameter fixed to its MC fitted values and by changing the (n, α) parameters by one standard deviation in a mode specific way.

- Change in background modeling. Instead of a fifth order polynomial, the data were fitted with a fourth and a sixth order polynomial. The background was also changed by fixing the amount of BG1 background described in Section 3.5.

The results are summarized in Table 4.9. The statistical error, from Table 4.4, is 2.3%. The assigned systematic N_{tag} error is 2.0%.

In principle various cuts, most notably particle ID cuts, do not produce directly a systematic error, as they only change the number of available tags. The Appendix

discusses K_s^0 cuts, where it is shown that backgrounds decrease by a factor of 4, when applying CLEANV0 cuts. Charged particle ID cuts are estimated on the signal side in Section 6.3.

Table 4.9: Summary of tag bias errors on N_{tag}.
Summary of tag bias errors on N_{tag}. First column: tag mode. Second column: nominal fitting. Third column: 4th order background polynomial. Fourth column: 6th order background polynomial. Fifth column: Crystal Ball paramenter n fixed at -3.14. Sixth column: Mode specific change of Crystal ball parameters (n, α) by a quantity of order of their fitted error. Seventh column: BG1 parameter fixed.

Mode	5th O.B.	4th O.B.	6th O.B.	Fix. n	Mode	Fix. BG1
401	15467±271	15268±377	15260±416	15529±333	15750±341	15990±247
400	3442±138	3456±132	3314±162	3457±140	3547±140	3535±96
440	2355±187	2348±174	2150±204	2367±187	2351±195	2506±210
460	1717±142	1662±132	1701±204	1720±146	1757±146	1634±83
421	4595±298	4360±1477	4934±412	4687±304	4784±303	4666±208
406	1707±94	1710±93	1751±153	1718±120	1739±96	1720±82
441	3607±640	3596±653	3343±868	3623±586	3606±611	3896±285
480	3373±248	3395±681	4240±472	3424±326	3454±328	3271±332
Tot.	36441	35795	36693	36525	36988	37218
Var.	-	-1.8%	+0.7%	+0.2%	+1.5%	+2.1%

4.5.3 Efficiency Errors.

Errors listed here comprise all effects which may affect the overall evaluation of the efficiency. The results are summarized in Table 4.10.

Omega branching ratio uncertainty: 0.8% [14].

Tracking efficiency error: 0.3% Gaussian systematic error per tag track, to be added linearly, totaling 0.9% per event. This systematic error is taken in accordance to Ref.[49]. It is not the same error as quoted in the Syracuse paper[50], which estimates a 2.7% error. It is noted that the 2.7% error is estimated using $K_s^0 K$ tags without using CleanV0.

Table 4.10: Summary of statistical and systematic errors of ϵ.
Summary of statistical and systematic errors of ϵ. The second column, labeled δ, is the shift in the central value due to a systematic effect. The third column, labeled σ, is the error associated with such effect.

Type	$\delta(\epsilon)/\epsilon$ (%)	$\sigma(\epsilon)/\epsilon$ (%)	Comment
Statistical	0	2.9	GENMC statistics
ω B.R.	-	0.8	Ref. [14]
Tracking	-	0.9	3 tracks
Electron eff.	-1.1	0.6	Ref. [41]
π^0 eff.	-6.4	2.3	Ref. [42]
π^0 cut variation	-	0.5	
MC form factor	-	0.5	
Extra track cut	-	0.04	
Particle ID	-	0.1	

π^0 reconstruction efficiency error. The π^0 spectra for $D_s \to \eta e\nu$, $D_s \to \phi e\nu$, and $D_s \to \omega e\nu$ are shown in Fig. 4.12. The MC significantly overestimates the π^0 reconstruction efficiency across the entire momentum spectrum. This systematic error was investigated in Ref. [42]. Table 11 of Ref. [42] gives a linear fit for the correction factor as a function of π^0 momentum with linear parameters

$$a_0 = (0.939 \pm 0.022),\ a_1 = (0.001 \pm 0.021),\ \rho = -0.947.$$

These parameters are a best fit for π^0 standard cuts, which are not completey equivalent to those discussed in this note.

Our cuts are different from standard π^0 cuts because one photon is required to have $E_\gamma > 30$ MeV, and to be in the good Barrel or End Cap region. To estimate the size of the systematics induced by this discrepancy, we analyzed the signal MC with and without these cuts. There were 41269 reconstructed events according to our cuts, and 41868 according to our cuts, a difference of 1.5%. There were 101 events instead of 99 in the combined η and ϕ peaks, a difference of 2%. We assumed a further 0.5% systematic error, listed in Table 4.10.

Correlated Gaussian pairs a_0, a_1 can be generated in the toy MC and convoluted with the π^0 energy distribution from the Signal MC (Fig. 4.12) to obtain the efficiency correction and its uncertainty.

Electron reconstruction efficiency error. The electron spectra for $D_s \to \eta e\nu$, $D_s \to \phi e\nu$, and $D_s \to \omega e\nu$ are shown in Fig. 4.12. The MC significantly overestimates the electron reconstruction efficiency, mostly at lower electron energies. This systematic error was investigated in Ref. [41]. Table 37 from Ref. [41] is used, which corresponds to the estimated electron efficiencies for the semileptonic decay $D^+ \to \omega e^+\nu$ at $\sqrt{s} = 3770MeV$. The corrections of Table 37 are convoluted with the electron momentum distribution from Fig. 4.12 to obtain the efficiency correction and its uncertainty. Note that the overall correction factor given in Table 4.10, which is 0.989, disagrees with the overall correction factor from Ref. [41], which is 0.986. The discrepancy is due to the more energetic electron spectrum at the higher energy and higher charmed meson mass in this analysis.

No extra track cut. Eliminating this cut from the signal MC analysis increases the number of accepted events from 41269 to 41287. The events in the η and ϕ peaks remain the same 99 events when this cut is removed. Given the small difference, we assign an error of 0.04% to this systematics.

Particle ID. By replacing the π identification cut used in the current analysis with a simple 3σ dEdx cut, the number of accepted signal MC events varies from 41269 to 41309. The events in the η and ϕ peaks remain the same 99 events when this cut is changed. Given the small difference, we assign an error of 0.1% to this systematics.

Form factor shape. A different form factor will change the efficiency, mostly because events with low Q^2 produce lower energy electrons. To evaluate this source of systematics, we assigned two weights

$$w_{\pm i}(Q_i^2) = 1 \pm 0.4(Q_i^2 - 0.7)/1.4$$

to each reconstructed event. The effect of the riweighing procedure is to change the $Q^2 = 0$ point and the approximate end point by $\pm 20\%$. The calculated new efficiencies are

$$\epsilon_{\pm} = \frac{\Sigma_{Nrec} w_{\pm i}}{\Sigma_{Ntot} w_{\pm i}}.$$

The new efficiencies are 5.49% and 5.55% respectively, to be compared to the given value of 5.52%. A systematic error of 0.5% is assigned to this systematics.

4.5.4 Toy Monte Carlo.

To obtain the final result, the Gaussian errors of ϵ and N_{tag} are convoluted with the non-Gaussian signal S distribution given by the likelihood(Fig. 4.10), by means of a toy Monte Carlo.

The procedure is indicated for two reasons. First, the main source of error, the unbinned likelihood, is non-Gaussian, whereas the smaller sources of error can be treated as Gaussian. Second, some sources of error shift the central value of the likelihood, an effect which can be treated exactly by shifting the likelihood on an event-by-event basis.

1×10^7 toy experiments are then generated, to obtain the final limit in Fig. 4.13.

4.6 Cross checks.

The parallel Rochester and Syracuse analyses offer the possibility of cross checks.

First, we compare the tag yields for the Rochester and WSU analyses in Table 4.11. This comparison is better than the comparison against the Syracuse analysis, because the more restrictive cuts on K_s can change the yields of modes 400 and 406.

Table 4.11 shows a side-to-side comparison of the calculated efficiencies for the

Rochester and WSU analyses, in the three semileptonic channels being considered.

Table 4.11: Rochester and WSU analyses. Tag efficiencies comparison.

Mode	Single tag		$\eta e\nu$		$\phi e\nu$		$\omega e\nu$
	WSU	Rochester	WSU	Rochester	WSU	Rochester	WSU
$K_s^0 K^-$	21.01	21.27	5.27	5.28	4.89	4.74	4.44
$K^+K^-\pi^-$	26.73	28.04	6.41	6.74	6.06	5.84	5.55
$K^{*-}K^{*0}$	12.08	12.17	2.59	2.68	2.62	2.41	2.39
$\pi^+\pi^-\pi^-$	38.42	38.62	9.76	9.79	9.13	8.83	8.44
$\eta\pi^-$	33.11	33.32	8.30	8.29	7.88	7.66	7.39
$\eta\rho^-$	14.89	14.56	3.45	3.57	3.45	3.29	3.10
$\pi^-\eta'(\eta\pi^+\pi^-)$	20.36	20.76	4.93	4.96	4.69	4.51	4.59
$\pi^-\eta'(\rho\gamma)$	28.19	28.15	6.95	6.89	6.54	6.02	6.03

Second, we have compared the final event samples obtained in our analysis and in the Rochester analysis. In the η mass region (30 MeV mass window, centered at the nominal η mass), we find 57 events in 8 tag channels, and Rochester finds the same 57 events plus one. In the ϕ mass region (40 MeV mass window, centered at the nominal ϕ mass) both analyses find the same 42 events.

Third, the ratio of branching ratios $\Gamma(D_s \to \eta e\nu)/\Gamma(D_s \to \phi e\nu)$ obtained in this analysis (statistical errors only) is 1.244 ± 0.219, to be compared with the Rochester result, which has a central value of 1.255.

Fourth, a comparison in the number of tags between the WSU analysis and the Syracuse analysis (Table below) shows a somewhat lower number of tags for our analysis, but in a consistent way. It is noted that this analysis is dominated by backgrounds, and that slightly stricter cuts are justified. It is also noted that the Syracuse MM^{*2} cuts are broader than the WSU cuts.

Further, so long as the MC simulates this selection precisely, the difference in yields does not generate a systematic error.

Table 4.12: WSU-Syracuse comparison of $Ntag$ yields.

Modes	WSU	Syracuse
$K_s^0 K^-$	3442 ± 138	4215 ± 128
$K^+ K^- \pi^-$	15647 ± 271	16087 ± 373
$K^{\star -} \bar{K^{\star 0}}$	1707 ± 94	2352 ± 176
$\pi^+ \pi^- \pi^-$	4595 ± 298	5014 ± 402
$\eta \pi^-$	2355 ± 187	2005 ± 145
$\eta \rho^-$	3606 ± 640	3295 ± 425
$\pi^- \eta'(\eta \pi^+ \pi^-)$	1716 ± 142	1647 ± 131
$\pi^- \eta'(\rho \gamma)$	3373 ± 240	2802 ± 227
$Ntag$	364411 ± 844	37417 ± 786

4.7 Conclusion.

In conclusion, the upper limit for the decay $D_s \to \omega e \nu$ was measured to be 0.231% at the 95% CL. The limit does not exclude the $\omega - \phi$ mixing model [34], which is $(0.13 \pm 0.05)\%$.

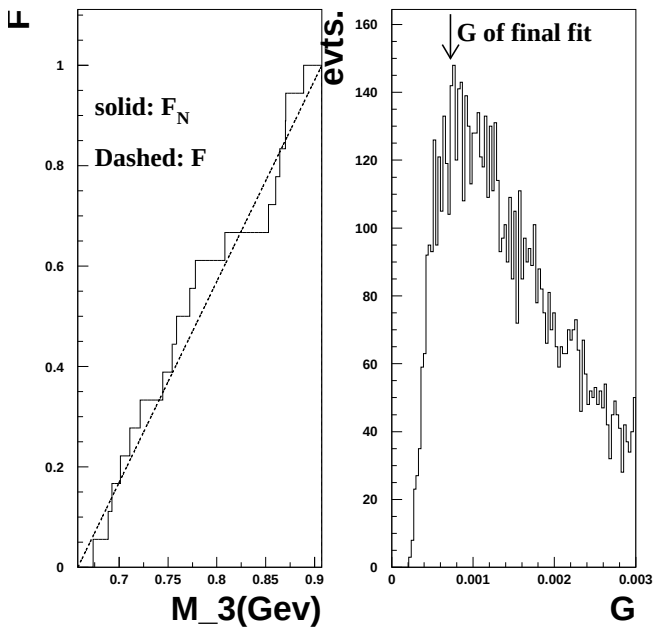

Figure 4.11: Cramer-Von Mises test of goodness of fit, for the final fit of this analysis. Left: comparison of the integrated probability distribution, F, and the step function F_N described in the text. Right: comparison of the G obtained in this analysis, with a distribution obtained from 10^4 unbiased toy Monte Carlo fits.

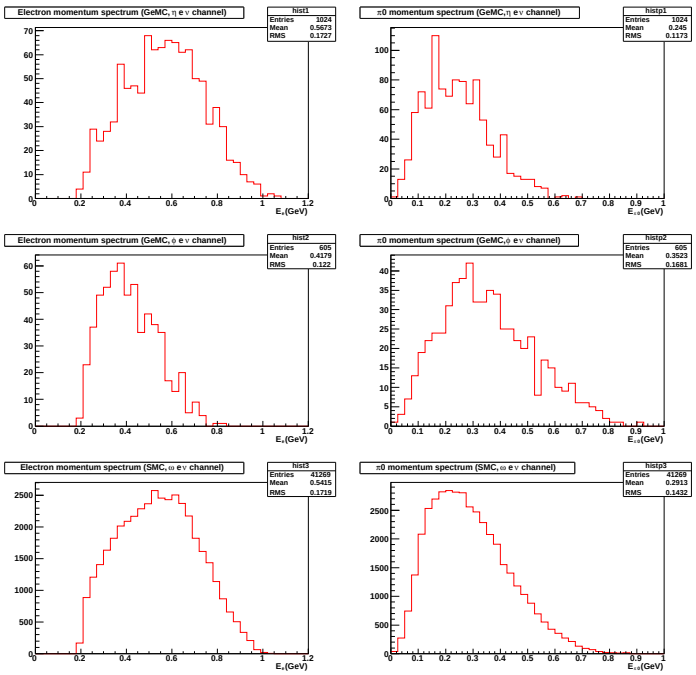

Figure 4.12: Electron and π^0 Monte Carlo momentum spectra. First column: electron momentum spectra. Second column: π^0 momentum spectra. First row: $D_s \to \eta e\nu$. Second row: $D_s \to \phi e\nu$.Third row: $D_s \to \omega e\nu$.

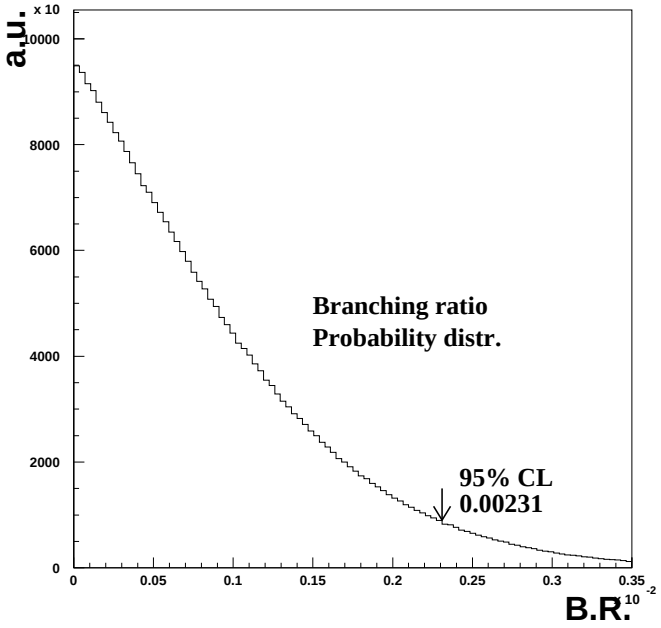

Figure 4.13: Final probability distribution for the Branching ratio, after convolution of all statistical and systematic errors, as described in the text.

REFERENCES

[1] S. L. Glashow. *Nucl. Phys.*, 22:579, 1961.

[2] S. Weinberg. *Phys. Rev. Lett.*, 19:1264, 1967.

[3] A. Salam. *Elementary Particle Theory.* N. Svartholm, ed., Stockholm: Almguist and Wiksell, 1968.

[4] D. J. Gross and F. Wilczek. *Phys. Rev. Lett*, 30:1343, 1973.

[5] H. D. Politzer. *Phys. Rev. Lett*, 30:1346, 1973.

[6] E. Noether. *Math. Phys.*, pages 235–257, 1918.

[7] T. D. Lee and C.N. Yang. *Phys. Rev.*, 104:254–258, 1956.

[8] R.W. Hayward D.D. Hoppes C.S. Wu, E. Ambler and Hudson. *Phys. Rev.*, 105:4, 1957.

[9] B. J. Bjorken and S.L. Glashow. *Physics Letters*, 11:255–257, 1964.

[10] N. Cabibbo. *Phys. Rev. Lett.*, 10:531–533, 1963.

[11] J. Iliopoulos S. L. Glashow and L. Maiani. *Phys. Rev. D*, 2:1285, 1970.

[12] M. Kobayashi and T. Maskawa. *Progr. Theor. Phys.*, 49:652–657, 1973.

[13] L. Wolfenstein. *Phys. Rev. Lett.*, 51:21, 1983.

[14] C. Amsler *et al. Physics Letters B*, 667:1, 2008.

[15] J.J. Aubert *et al. Phys. Rev. Lett.*, 33:1404, 1974.

[16] J.E. Augustin *et al*. *Phys. Rev. Lett.*, 33:1406, 1974.

[17] G. P. Lepage and S. J. Brodsky. *Phys. Rev. D*, 22:2157–2198, 1980.

[18] S. J. Brodsky *et al*. *Phys. Rept.*, 301:299–486, 1998.

[19] K. Abe *et al*. *Phys. Rev. Lett.*, 98:082001, 2007.

[20] B. Aubert *et al*. *Phys. Rev. D*, 73:011101, 2006.

[21] Q. He *et al*. *Phys. Rev D*, 74:091104, 2006.

[22] S. K. Choi *et al*. *Phys. Rev. Lett.*, 100:142001, 2008.

[23] F. E. Close and P. R. Page. *Physics Letters*, B578:219, 2003.

[24] M. B. Voloshin. *Phys. Lett.*, B579:316, 2004.

[25] N. A. Torngvist. *Physics. Letters*, B590:209, 2004.

[26] E. S. Swanson. *Physics Letters*, B588:189, 2004.

[27] E. Braaten and M. Kusunoki. *Phys. Rev. D*, 69:114012, 2004.

[28] C. Y. Wong. *Phys. Rev. C*, 69:055202, 2004.

[29] I. Bigi *et al*. *Phys. Rev. D*, 72:114016, 2005.

[30] L. Maiani *et al*. *Phys. Rev. D*, 72:031502, 2005.

[31] T. W. Chiu and T. H. Hsieh. *Physics Letters*, B646:205, 2007.

[32] G. Bonvinici. Proceedings of workshop on the transition from low to high q form-factors (to honor the occasion of the 60th birthday of stanley brodsky). Athens, GA, 17 Sep 1999.

[33] Jian-wei Qiu F. Gabbiani and G. Valencia. *Phys. Rev. D*, 66:114015, 2002.

[34] M. Gronau and J. Rosner. *Phys. Rev. D*, 79:074006, 2009.

[35] CESR and CLEO staff. *CLNS 93/1265, Laboratory for Elementary-Particle Physics*, volume Publication (1993).

[36] Y. Kubota *et al*. *NIM*, A320:66, 1992.

[37] R. A. Briere *et al*. Cleo-c and cesr-c: A new frontier of weak and strong interactions. *CLNS*, 1/1742.

[38] M. Artuso *et al*. *NIM*, A554:147–194, 2005.

[39] D. Cronin-Hennessy *et al*. *Phys. Rev. D*, 80:072001, 2009.

[40] W. Sun P. Onyisi S. Stroiney, A. Ryd and D. Cassel. *CBX*, 2008-040.

[41] C. S. Park and E. H. Thorndike. *CBX*, 2008-049.

[42] L. Fields and R. Patterson. *CBX*, 2008-029.

[43] W. Sun P. Onyisi S. Stroiney, A. Ryd and D. Cassel. *CBX*, 2008-041.

[44] S. Stroiney and W. Sun. *CBX*, 2006-11.

[45] C. P. Prescott. *CSN 97/353*.

[46] J. Fast *et al*. *CBX*, 98-41.

[47] T. W. Anderson. *Ann. Math. Statist*, 33, 3, 1962.

[48] F. Yang and E. D. Thorndike. *CBX*, 2009-010.

[49] B. Xin and I. Shipsey. *CBX*, 2008-027.

[50] S. Stone and L. Zhang. *CPDRAFT*, 2009-011.

ABSTRACT

SEARCH FOR THE DECAY
$Ds \rightarrow \omega\ l\ \nu$

by

JIN ZHU

May 2010

Advisor: Dr. Giovanni Bonvinici

Major: Physics

Degree: Doctor of Philosophy

This analysis searches for a new type of rare decay of the charmed mesons, which would provide direct evidence for the presence of Fock states inside hadrons.

We use 586pb^{-1} of e^+e^- collisions at the Cornell Electron Storage Ring (CESR), at $\sqrt{s} = 4.17$ GeV, recorded with the Cleo-c detector.

A limit on the branching ratio $D_s \rightarrow \omega e\nu$ is found, at 0.231% (95% C.L.).

AUTOBIOGRAPHICAL STATEMENT

Name: Jin Zhu

Education:

M.S. Science in theoretical physics, Institute of High Energy Physics, Chinese Academy of Science, Beijing, China, 2006

B.S. Science in applied physics, Tianjin University, Tianjin, China, 2003

Professional experience:

Postdoc: William Beaumont Hospital, Royal Oak, Michigan, 2009

Publication:

1. C.D. Lu, Y.L. Shen and J. Zhu, $B^0 \to \phi\phi$ decay in Perturbative QCD Approach. Eur. Phy. J. C 41 311, 2005.

2. J. Zhu, Y.L. Shen and C.D. Lu, Polarization, CP Asymmetry and Branching ratios in $B \to KK$ with Perturbative QCD approach. Phy. Rev. D 72 054015, 2005.

3. J. Zhu, Y.L. Shen and C.D. Lu, $B_s \to \phi(\omega)K$ with Perturbative QCD approach. J. Phys. G: Nucl Part. 32 101, 2006.

4. H.W. Huang, T. Morii, J. Zhu and et. al, Study of $B \to K\rho$ & $K\omega$ with polarization. Phy. Rev. D 73 014011, 2006

5. J. Zhu, G. Bonvicini and et. al, Search for the decay $Ds \to \omega l\nu$, In preparation.

6. J. Zhu, T. Zhang, R. Hazel, D. Drake and D. Yan, Automatic Linac Quality Assurance (QA) with Electronic Portal Imaging Device(EPID), submitted to medical physics.

7. J. Zhu, J. Liang and D. Yan, Interplay study between respirationmotion and dynamic MLC delivery for 4D IMRT plan. Submitted to AAPM 2010 annual meeting.